



Quasilinear transport modelling at low magnetic shear

J. Citrin, C. Bourdelle, P. Cottier, D. F. Escande, Ö. D. Gürcan et al.

Citation: [Phys. Plasmas](#) **19**, 062305 (2012); doi: 10.1063/1.4719697

View online: <http://dx.doi.org/10.1063/1.4719697>

View Table of Contents: <http://pop.aip.org/resource/1/PHPAEN/v19/i6>

Published by the [AIP Publishing LLC](#).

Additional information on Phys. Plasmas

Journal Homepage: <http://pop.aip.org/>

Journal Information: http://pop.aip.org/about/about_the_journal

Top downloads: http://pop.aip.org/features/most_downloaded

Information for Authors: <http://pop.aip.org/authors>

ADVERTISEMENT

An advertisement banner for AIP Advances. The top part features the 'AIP Advances' logo, which includes the text 'AIP Advances' in a green font and a series of orange and yellow circles of varying sizes arranged in an arc above the text. The background of the banner is a green and white abstract pattern of curved lines. Below the logo, the text 'Special Topic Section:' is written in white, followed by 'PHYSICS OF CANCER' in a large, bold, white font. At the bottom, the text 'Why cancer? Why physics?' is written in a green font, and a blue button with the text 'View Articles Now' is positioned to the right.

AIP Advances

Special Topic Section:
PHYSICS OF CANCER

Why cancer? Why physics? [View Articles Now](#)

Quasilinear transport modelling at low magnetic shear

J. Citrin,^{1,a)} C. Bourdelle,² P. Cottier,² D. F. Escande,³ Ö. D. Gürçan,⁴ D. R. Hatch,⁵
G. M. D. Hogewij,¹ F. Jenko,⁵ and M. J. Pueschel⁵

¹FOM Institute DIFFER—Dutch Institute for Fundamental Energy Research, Association EURATOM-FOM, Nieuwegein, The Netherlands

²CEA, IRFM, F-13108 Saint Paul Lez Durance, France

³UMR 6633 CNRS-Université de Provence, Marseille, France

⁴Laboratoire de Physique des Plasmas, Ecole Polytechnique, CNRS, 91128 Palaiseau Cedex, France

⁵Max-Planck-Institut für Plasmaphysik, EURATOM Association, D-85748 Garching, Germany

(Received 19 January 2012; accepted 4 April 2012; published online 8 June 2012)

Accurate and computationally inexpensive transport models are vital for routine and robust predictions of tokamak turbulent transport. To this end, the QuaLiKiz [Bourdelle *et al.*, Phys. Plasmas **14**, 112501 (2007)] quasilinear gyrokinetic transport model has been recently developed. QuaLiKiz flux predictions have been validated by non-linear simulations over a wide range in parameter space. However, a discrepancy is found at low magnetic shear, where the quasilinear fluxes are significantly larger than the non-linear predictions. This discrepancy is found to stem from two distinct sources: the turbulence correlation length in the mixing length rule and an increase in the ratio between the quasilinear and non-linear transport weights, correlated with increased non-linear frequency broadening. Significantly closer agreement between the quasilinear and non-linear predictions is achieved through the development of an improved mixing length rule, whose assumptions are validated by non-linear simulations. © 2012 American Institute of Physics. [<http://dx.doi.org/10.1063/1.4719697>]

I. INTRODUCTION

The availability and accuracy of computationally inexpensive first-principle physics based transport codes is vital for both interpretation of tokamak experiments and extrapolation to future devices. With this goal in mind, the QuaLiKiz quasi-linear transport model has been developed.¹ Particle and heat flux calculation time in QuaLiKiz is $\sim 50\,000$ less than in local non-linear codes. Fluxes computed by QuaLiKiz have been validated by non-linear GYRO^{2,3} simulations over a wide range of parameter space.⁴ However, significant discrepancies between QuaLiKiz and non-linear simulations have been observed at low magnetic shear.

The successful prediction of transport in the low magnetic shear regime is important for the interpretation of advanced tokamak scenarios, as has been recently seen in JET hybrid scenarios at combined low magnetic shear and high rotational shear.⁵ Low magnetic shear regions are also expected during ramp-up and ramp-down phases. For extrapolation to ITER, transport at low magnetic shear is important for all scenarios. This is due to the fact that in ITER, the sawtooth period is expected to be an order of magnitude greater than the confinement time.⁶ Therefore, even in the ITER reference H-mode scenario, low magnetic shear transport within the inversion radius between sawtooth crashes will be critical for determining the average fusion power.

The primary motivation of this work is thus to understand the physics behind the low magnetic shear discrepancy between the QuaLiKiz model as formulated in Casati *et al.*,⁴

and non-linear simulations. To this end, the assumptions made in the QuaLiKiz model are systematically examined at low magnetic shear. Both linear and non-linear simulations with the gyrokinetic code GENE⁷ have been used extensively for comparisons and assumption validation.

The structure of the paper is as follows. In Sec. II, the QuaLiKiz model is reviewed and the discrepancy compared to non-linear simulations at low magnetic shear is introduced. In Sec. III, a review of basic understandings of the magnetic shear impact on linear modes is presented. QuaLiKiz and GENE linear growth rates are compared at low magnetic shear, and the differences between them are not sufficient to explain the flux discrepancy. In Sec. IV, QuaLiKiz assumptions on non-linear effects are explored. The validity of the quasi-linear approximation itself with regard to the ordering of the non-linear characteristic times (Kubo numbers) is examined and is found to still hold at low magnetic shear. The delicate choice of electrostatic potential saturation level, through the mixing length rule and frequency broadening, is reevaluated at low magnetic shear. The assumptions behind the saturated potential formulation have been reexamined in great detail with the aid of 16 non-linear GENE simulations at various values of magnetic shear, q-profile, and driving gradient lengths. Partial isotropization of turbulent eddies, radial correlation length dependence on the magnetic shear, and increased resonance broadening at low magnetic shear are all observed. These observations are taken into account in the quasilinear model, and agreement with the non-linear magnetic shear scans is much improved. Conclusions are discussed in Sec. V.

A number of more technical aspects have been summarized in appendixes. In Appendix A, the analytical fluid limit

^{a)}Electronic mail: J.Citrin@differ.nl.

applied in the QuaLiKiz Gaussian eigenmode ansatz is reviewed. In Appendix B, the locality assumption is examined at low magnetic shear and found to hold for $|s| > 0.1$. In Appendix C, the validity of the QuaLiKiz eigenmode ansatz is examined at low magnetic shear, through comparisons with self-consistent mode structure calculations from linear-GENE. This QuaLiKiz assumption was also found to hold for $|s| > 0.1$. Recent improvements in the QuaLiKiz linear solver are summarized in the remaining appendixes: treatment of the bounce average and bounce frequency resonance in the trapped particle functional (Appendix D), mode width calculation in $k_\theta \rho_s \gg 1$ electron temperature gradient (ETG) relevant wavenumbers (Appendix E), and mode width calculation in the vicinity of $s \sim 0.5$ (Appendix F).

Many of the simulations carried out in this work refer to ‘GA-standard case’ parameters. For reference, we list these parameters here: $r/a = 0.5$, $R/L_{Ti,e} = 9$, $R/L_n = 3$, $q = 2$, $T_i/T_e = 1$, $s = 1$, $\beta = 0$, and $\nu^* = 0$.

Finally, we clarify here the wavenumber notation used in this work. k_y is the wavenumber, normalized to $1/\rho_s$, corresponding to the binormal coordinate y in the GENE field-aligned coordinate system. In QuaLiKiz, k_θ is used, which corresponds to the wavenumber in the poloidal direction. For all parameters studied in this work, k_y differs from $k_\theta \rho_s$ by at most 2%. Thus for convenience, we will not differentiate between the two, and henceforth always use k_y in reference to all simulation results.

II. REVIEW OF THE QUALIKIZ MODEL

QuaLiKiz is based on the electrostatic eigenvalue gyrokinetic code Kinezero,⁸ which includes two ion species and both passing and trapped electrons. For the minimization of computational expense—critical for integrated modelling applications—the electrostatic potential shape is not calculated self-consistently. Rather, an analytical solution obtained in the fluid limit is taken, and the strong ballooning representation limit applied. A Krook-like collision operator accounting for the impact of collisions on the trapped electrons has also been included.⁹ Shifted circle ($s - \alpha$) geometry is assumed for equilibrium.

The linear response calculated by Kinezero has been incorporated into the gyrokinetic quasilinear expressions for the particle and heat fluxes, resulting in the QuaLiKiz transport model.¹ From henceforth, we will also refer to the eigenvalue solver as part of ‘the QuaLiKiz model.’ The fluxes can be schematically decomposed into contributions of the linear response and the saturated electrostatic potential

$$\Gamma, Q_i, Q_e = \sum_{k_\theta, \omega, \omega_{kj}} \text{Im}(R_{lin}^{\Gamma, Q_i, Q_e}(k_\theta, \omega, \omega_{kj})) |\delta\phi(k_\theta, \omega, \omega_{kj})|^2, \quad (1)$$

where $R_{lin}^{\Gamma, Q_i, Q_e}$ is the linear response for the density, ion temperature, and electron temperature fluctuations respectively, $\delta\phi$ the saturated electrostatic potential, ω the fluctuation frequency, and ω_{kj} the eigenfrequency of the unstable mode with poloidal wavenumber $k_\theta = nq/r$. Multiple instabilities may coexist with the same k_θ and are discriminated by the

index j . The contribution of each unstable mode (also named ‘branches’) to the fluxes are summed over. The linear response has been extensively validated by comparison with non-linear simulations.^{4,10}

The model for the saturated electrostatic potential—a critical ingredient in evaluating the turbulent fluxes—consists of a mixing length rule weighted by a k-space spectral function validated against both non-linear simulations and experimental observations.^{4,11} The saturated potential frequency spectral shape is taken as a Lorentzian, with a width equal to the linear growth rate. This assumption has been shown to agree with non-linear simulations and experimental observations at transport relevant wavelengths.¹⁰ Finally, the QuaLiKiz predicted fluxes are normalized by a single, constant, fitting coefficient, set such that the ion heat flux predicted by QuaLiKiz for the GA-standard case agrees with GYRO predictions.

The mixing length rule as previously applied in QuaLiKiz is now presented. We redefine for convenience the saturated electrostatic potential for each mode as $|\delta\phi_{k,j}|^2$, where k is the wavenumber index and j the branch index. We assume $|\delta\phi_{k,j}|^2 = S_{kj} L_j$, where S_{kj} is a branch dependent k-space spectral function shape, and L_j is the maximum mixing length amplitude for branch j : $L_j \equiv |\frac{\gamma_{kj}}{(k_\perp^2)}|_{max}$. The maximum is taken over the k-spectrum. The k_θ corresponding to the maximum is denoted $k_\theta|_{max}$ and represents the peak of the flux spectrum defined by S_{kj} , designed to reproduce the downshifted non-linear flux spectrum.¹² S_{kj} is taken such that $S_{kj} \propto (k_\theta)^3$ for $k_\theta < k_\theta|_{max}$ and $S_{kj} \propto (k_\theta)^{-3}$ for $k_\theta > k_\theta|_{max}$. $\langle k_\perp^2 \rangle = k_\theta^2 (1 + (s - \alpha)^2 \langle \theta^2 \rangle)$, where $\langle \rangle$ denotes a poloidal average. This average over the ballooning structure, when integrating over the form imposed by the fluid Gaussian eigenmode assumption, is given by $\langle \theta^2 \rangle = \frac{2d^2 \Gamma(3/4)}{w^2 \Gamma(1/4)}$. d is the distance between rational surfaces and w is the mode Gaussian width. This choice of k-space spectrum is in agreement with nonlinear simulations and observations.^{4,11}

Fluxes computed by QuaLiKiz have been compared with GYRO non-linear simulations, and agreement for both heat and particle fluxes have been obtained in R/L_T , Z_{eff} , T_i/T_e , and collisionality scans around GA-standard case parameters.⁴ Extensive GYRO non-linear simulations consisting of q-profile and magnetic shear scans have previously been carried out.¹³ In Figure 1, the R/L_T scan comparison is reproduced, and q-profile and magnetic shear scans around the GA standard case have been added. The q-profile scan also shows agreement between the predictions. However, significant discrepancies between QuaLiKiz and GYRO are evident in the magnetic shear scan, in the region $|s| < 0.5$. Note that $\alpha = 0$ in all these calculations. We now set out to uncover the sources of this discrepancy.

III. MAGNETIC SHEAR IMPACT ON LINEAR PHYSICS

In this section, we review linear growth rate dependence on magnetic shear and compare QuaLiKiz and linear-GENE growth rate calculations. Both the role of the magnetic shear on the R/L_{Ti} thresholds of ion temperature gradient (ITG) instabilities and on γ -stiffness is discussed. γ -stiffness is

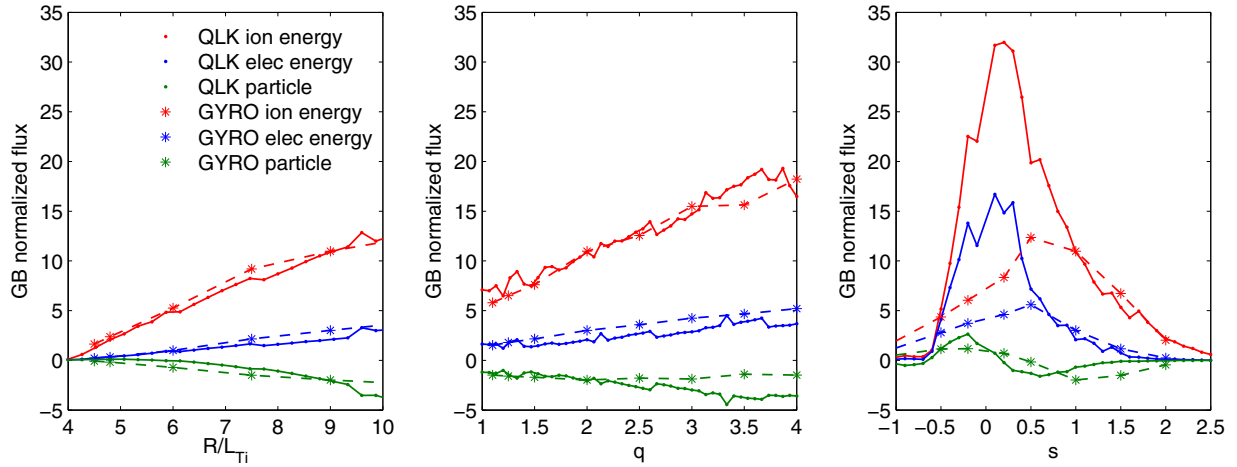


FIG. 1. Energy and particle fluxes, compared between GYRO and QuaLiKiz for 3 scans around the GASTD case: R/L_T (left panel), q (central panel), and s (right panel). This comparison is with the previous mixing length formulation in QuaLiKiz as presented in Casati *et al.*⁴

defined as the rate of change of the growth rate as a function of the driving gradient lengths. In Sec. III A, analytical and computational results for the ITG instability threshold are briefly reviewed. While in the fluid limit, we expect higher growth rates for higher s/q (see Appendix A), the linear thresholds of the ITG modes are in fact expected to decrease with s/q . This points to reduced γ -stiffness at low magnetic shear. Particularly, the toroidal ITG branch modes at low $k_y s$ are stabilized. The analytical linear results are corroborated by computations with both linear-GENE and QuaLiKiz. The agreement between dominant branch growth rate calculations in linear-GENE and QuaLiKiz is satisfactory at low magnetic shear. This leads to the conclusion that the reason for the discrepancy between the quasilinear and non-linear fluxes at low magnetic shear lies in the non-linear physics.

A. Linear thresholds from kinetic theory

In this section, we briefly review previous results of kinetic theory regarding magnetic shear dependences on threshold, for ITG turbulence. For the η_i ITG mode ($\eta_i \equiv d \ln T_i / d \ln n$), the R/L_{Ti} threshold has been calculated in the short-wavelength, flat density limit ($k_\theta \rho_s s \approx (L_T/R)^{1/4}$ and $R/L_n < 2(1 + T_i/T_e)$), as follows:¹⁵

$$(R/L_{Ti})_c \approx \frac{4}{3} (1 + T_i/T_e) \left(1 + 2 \frac{s}{q} \right). \quad (2)$$

Increasing the density gradient is predicted to lead to an increased R/L_{Ti} threshold. However, when including trapped electrons, the increased density gradient can destabilize the trapped electron mode (TEM) branch, nullifying the turbulence stabilization.¹⁶

A study of the (s, q) impact on the linear R/L_T threshold for ITG/TEM modes in Kinezero (and thus in QuaLiKiz) have previously been carried out with fixed $T_i/T_e = Z_{eff} = 1$, $\alpha = 0$ and in the flat density limit.¹⁷ The parameterization of the critical temperature gradient lengths, $(R/L_T)_c$, was as follows for ITG-like modes: $1.1 + 1.4 s + 1.9 s/q$ for $s > 0$ and $0.9 + 1.6|s| + 9.9|s|/q$ for $s < 0$. This mixed s and s/q dependency share the same qualitative dependencies as in

the analytical limits above. The asymmetry with the sign of s is due to the stabilization of the toroidal branch for negative shear. An extensive study of T_i/T_e dependence in QuaLiKiz was carried out by Casati *et al.*¹⁸

Finally, comprehensive linear gyrokinetic simulations with GS2 have led to a parameterization of ETG linear thresholds, isomorphic with ITG linear thresholds (assuming adiabatic electrons), for which it can be written as follows:¹⁹

$$(R/L_{Ti})_c = \max\{(1 + T_i/T_e)(1.33 + 1.91s/q)(1 - 1.5\epsilon) \times [1 + 0.3\epsilon(d\kappa/d\epsilon)], 0.8R/L_n\}, \quad (3)$$

where $\epsilon = r/R$ and κ is the elongation. In the circular cross-section limit, this formula is very similar to the analytical formula, Eq. (2).

Growth rate contour plots calculated by QuaLiKiz are shown in Figure 2. The growth rates correspond to the most unstable branch in GA-standard R/L_T and magnetic shear scans (where $R/L_{Ti} = R/L_{Te}$). In the left panel, the maximum growth rate for the spectrum $k_y < 0.8$ is displayed. In the right panel, the growth rates for $k_y = 0.2$ are displayed. In both plots, the increased instability threshold for high magnetic shear and negative magnetic shear is clearly visible. The residual modes at low R/L_T at low magnetic shear are modes in the electron diamagnetic direction due to the finite R/L_n in the GA-standard case.

An interesting detail to note in the low k_y case (right panel) of Figure 2 is reduced γ -stiffness at low magnetic shear. This is evidenced by the significantly decreased gradient with respect to R/L_T at $s < 0.2$. A possible explanation for this decreased γ -stiffness is that the long-wavelength limit is reached, defined by $k_y s \ll (L_{Ti}/R)^{1/4}$. In this limit, the toroidal branch is stabilized.²⁰ This is due to the growth of the eigenfunction envelope width along the magnetic field, given by $\theta \approx s^{-1/2} \epsilon_r^{1/4} (k_\theta \rho_i)^{-1}$. A broad envelope leads to decreased interaction with the bad curvature region, stabilizing the toroidal branch. In the QuaLiKiz Gaussian eigenmode approximation, the envelope width is proportional to d/w , which increases at low k_y , and also increases at low magnetic shear as seen in Figure 5 in Romanelli

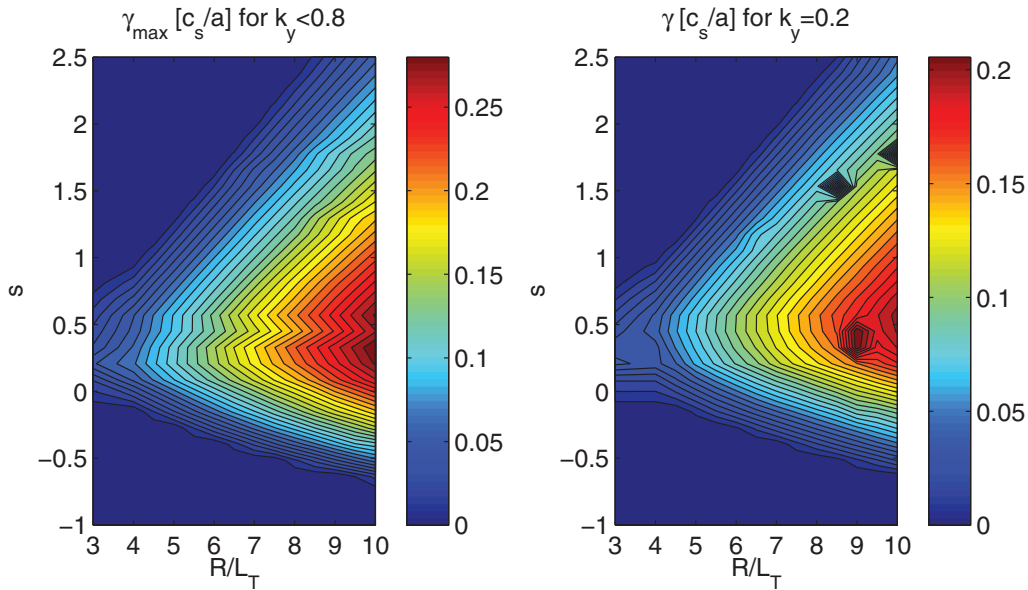


FIG. 2. Linear growth rates for the most unstable branch calculated by QuaLiKiz in a GA-STD R/L_T scan, where $R/L_{Ti} = R/L_{Te}$. In the left panel, the maximum growth rate for the spectrum $k_y < 0.8$ is shown. In the right panel, the growth rate for $k_y = 0.2$ is shown.

*et al.*⁹ Decreased linear growth rates at low $k_y s$ may lead to preferential quenching of long wavelength turbulence by zonal flows at low magnetic shear. Since these long wavelengths dominate the transport, this can play a major role in the determination of the fluxes.

B. Comparison of QuaLiKiz and linear-GENE growth rates

Growth rates of the dominant branch calculated by QuaLiKiz and GENE are compared in this section. In Figure 3, results of a R/L_T scan are displayed (where $R/L_{Ti} = R/L_{Te}$ throughout the scan), around the GA-standard case, at $k_y = 0.15$ and 0.3 and $s = 0.1$ and 1 . We can see that even though the R/L_T thresholds are lower for the lower shear cases, the γ -stiffness is also lower for the lower shear case, leading to a crossover of the high-shear and low-shear γ curves at a R/L_T position dependent on k_y . At low k_y , this crossing point is much closer to the threshold, at experimentally relevant

R/L_T . Note that this effect is predicted by both GENE and QuaLiKiz, in spite of the Gaussian eigenmode ansatz made in QuaLiKiz. Indeed, it is shown in Appendix C that this ansatz is valid down to $s = 0.1$ and $k_y = 0.15$.

We also show in Figure 4, a comparison between linear-GENE and QuaLiKiz of the growth rate calculation for a GA-standard magnetic shear scan at $k_y = 0.3$. The QuaLiKiz predictions agree with linear-GENE to within $\sim 30\%$ even at low magnetic shear. However, at negative magnetic shear, QuaLiKiz severely underpredicts the growth rates, due to an underestimation of the slab ITG branch growth rate. This may be due to the strong ballooning representation and prescribed eigenmode assumptions. The resolution of this issue is left for future work.

In summary, while the ITG threshold decreases at low magnetic shear, the γ -stiffness is also reduced at lower magnetic shear. At low k_y , this effect is increased. This is reproduced both by linear-GENE and QuaLiKiz. Furthermore, dominant branch linear-GENE and QuaLiKiz calculations

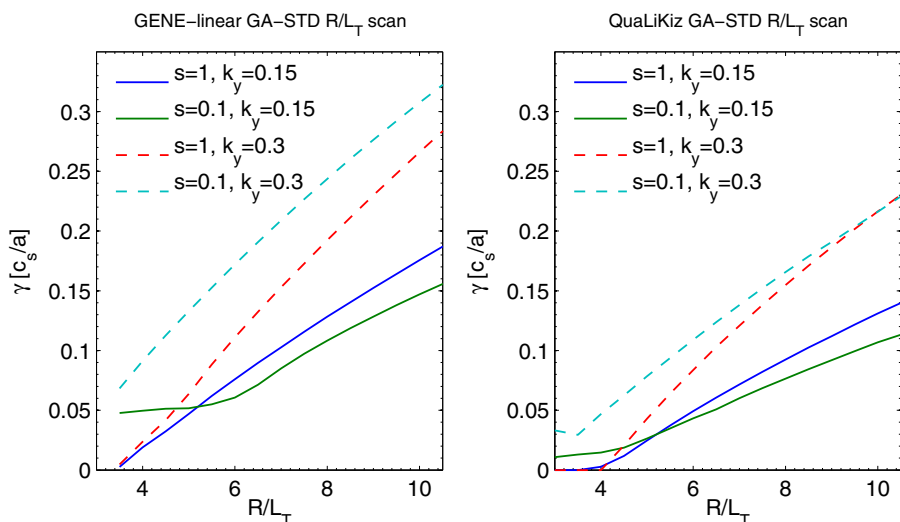


FIG. 3. Linear growth rates calculated for the GA-STD kinetic electron case in a R/L_T scan at various k_y and magnetic shear values by both linear-GENE (left panel) and QuaLiKiz (right panel).

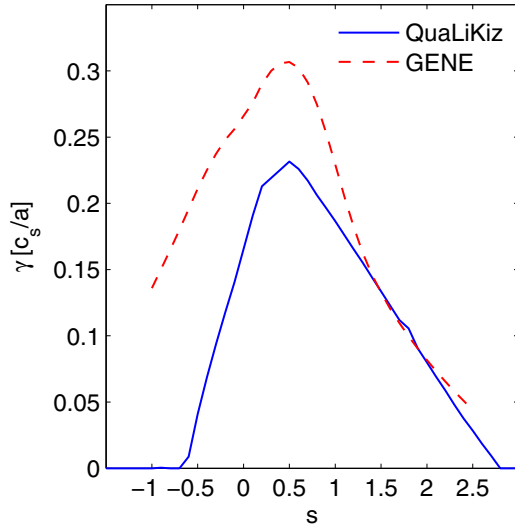


FIG. 4. Linear growth rates calculated for a magnetic shear scan around the GA-standard case by both QuaLiKiz (solid lines) and linear-GENE (dashed lines) for $k_y = 0.3$.

agree to within $\sim 30\%$ in the parameter ranges studied, in spite of the QuaLiKiz Gaussian eigenmode ansatz. Therefore, a miscalculation of the dominant branch growth rate cannot be responsible for the low magnetic shear flux discrepancy between QuaLiKiz and non-linear models, where the QuaLiKiz flux is significantly higher as seen in Figure 1. The reduced growth rates at combined low magnetic shear and low k_y are an important point, since this could have ramifications for setting the turbulence correlation length. This is explored further in the modification of the mixing length rule in Sec. IV C.

IV. NON-LINEAR EFFECTS AT LOW MAGNETIC SHEAR

In this section, we explore the non-linear physics, which may lead to the lack of validity of the previous QuaLiKiz quasilinear computed fluxes at low magnetic shear. As described in Sec. I, the quasilinear flux can be decomposed into two parts: the linear response and the saturated electrostatic

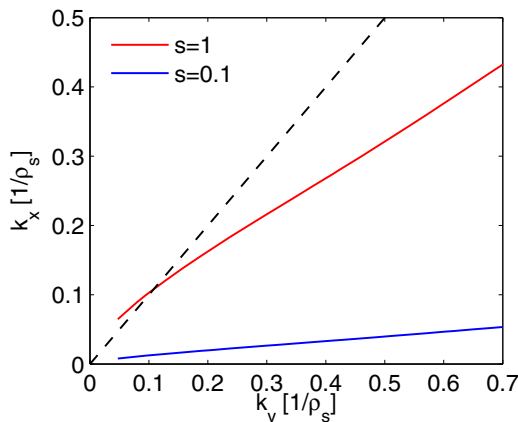


FIG. 5. k_x as a function of k_y , as calculated in QuaLiKiz for $s = 1$ and $s = 0.1$, from the k_\perp formulation given in Eq. (4). The dashed curve represents $k_x = k_y$, as a measure for the degree of isotropy.

potential. This description is justified if the particles undergo stochastic linearized trajectories. This assumption, central to quasilinear theory, can be verified by examining the ordering of the turbulence autocorrelation time compared to the eddy turnover time, as expressed through the Kubo number. This verification was done here for low magnetic shear. Furthermore, the QuaLiKiz mixing length model for the non-linear saturated potential was also reexamined at low magnetic shear. This includes the model for k_\perp , the evaluation of the k_y maximum of the non-linear flux spectrum, and the frequency broadening assumption. These assumptions were extensively validated previously for a wide range of parameters,⁴ but not for magnetic shear scans. We extend this validation towards low magnetic shear.

A set of dedicated GENE non-linear runs were carried out to test and validate the QuaLiKiz assumptions. These non-linear runs are introduced in Sec. IV A. In Sec. IV B, the evaluation of the Kubo numbers in the non-linear simulations is discussed. In Sec. IV C, the mixing length model for the saturated potential is reexamined and modified following comparisons with the non-linear simulations. Finally, predicted fluxes from both the modified QuaLiKiz and the set of non-linear GENE simulations are compared in Sec. IV D.

A. Description of GENE runs

A total of 16 non-linear GENE runs were carried out. The runs are comprised of 4 sets of 4-point magnetic shear scans at $s = -0.4, 0.1, 0.6$, and 1. The sets are comprised of the GA-standard case, and 3 further sets with lowered inverse gradient lengths and varying q-profile values, consistent with typical JET hybrid scenario parameters at mid-radius. This was done in order to widen the GENE-QuaLiKiz magnetic shear scan validation in q-profile parameter space, down towards $q = 1$, which often coincides with low magnetic shear in experiments. Furthermore, the added data sets allow GENE-QuaLiKiz validation at lower levels of flux than the GA-standard case. Since the eventual goal is to apply QuaLiKiz as a transport model within the integrated modelling framework, validation at more experimentally relevant fluxes is critical. The parameters for these sets are summarized in Table I. All GENE simulations carried out were electrostatic, local, collisionless, with periodic radial boundary conditions, kinetic electrons (and real mass ratio), and with $s - \alpha$ geometry. Throughout the sets, $\alpha = 0$, $r/a = 0.5$, and $R_0/a = 3$.

In all simulations, we used 16-point discretization in the parallel direction, 32 or 48-points in the parallel velocity directions (based on linear convergence studies), and 8 magnetic moments. For these parameters, non-linear convergence tests were carried out, and the heat flux sensitivities were negligible. For each simulation, extensive non-linear convergence

TABLE I. Input parameters for the GENE magnetic shear scans.

Set name	R/L_{Ti}	R/L_{Te}	R/L_n	T_i/T_e	q
A (GASTD)	9	9	3	1	2
B	7.6	6.7	4	1.4	1.4
C	6.3	5.5	3.3	1.4	1.4
D	7.6	6.7	4	1.4	1

studies were carried out in the number of toroidal modes, the perpendicular box sizes, and in the radial grid discretization. The box sizes in the perpendicular directions range from $[L_x/\rho_s, L_y/\rho_s] = [100, 126]$ for the set A, $s = 1$ case to up to $[L_x/\rho_s, L_y/\rho_s] = [333, 210]$ for the more challenging $s = 0.1$ cases. The number of toroidal modes (n_y) employed ranged from 16 for the set A, $s = 1$ case, to 32 for the $s = 0.1$ cases. The $n_y = 32$ cases correspond to $k_y(max) = 1.55$ or $k_y(max) = 0.93$, depending on the perpendicular box size. In general, the $s = 0.1$ cases were more computationally intensive due to the higher radial box size needed to satisfy the parallel boundary condition, and also due to the higher number of toroidal modes necessary for convergence.

Low heat flux sensitivity was also found to the inclusion of collisions. However, it was found that the particle transport was highly sensitive to the velocity and parallel space resolutions, particularly when a particle inward flux dominates (as in the set A, $s = 1$ case). This particle transport sensitivity was greatly decreased when including collisions. In general, verification of the QuaLiKiz particle transport predictions is also of great importance. However, it is preferable to carry out this verification vs non-linear runs when including collisionality. This is due both to the increased experimental relevance and also the seemingly improved non-linear convergence properties of particle diffusivity in collisional runs. Due to the increased computational expense of collisional runs, a more rigorous validation of the particle fluxes when including collisionality is deferred to future work. Here, we concentrate on the heat transport validation of the collisionless QuaLiKiz model at low magnetic shear and maintain a caveat on the convergence of the non-linearly calculated particle fluxes in this work, particularly the inward fluxes. The discretization and box size choices, as well as the transport predictions of all 16 runs, are shown in Table II.

B. Kubo numbers

The validity of the quasilinear assumption depends on whether test particles in the turbulent fields undergo stochastic

linearized trajectories, allowing a diffusive random-walk process to be considered as opposed to field trapping. This can be quantified by the Kubo number K ,^{21,22} the ratio between the Eulerian autocorrelation time, τ_{ac} , of the fluctuating potential and the particle flight time, τ_f . τ_f is defined as $\lambda_x/\langle v_x \rangle$, where λ_x is the radial correlation decay length, and $\langle v_x \rangle$ the root mean square radial velocity of a test particle in the turbulent field. For $K < 1$, the autocorrelation time of the turbulent field is shorter than the transit time of a test particle around a turbulent eddy, justifying the use of a random-walk diffusive model. This condition is however necessary but not sufficient. In addition, there must be enough randomness in the Hamiltonian described in the dynamics, e.g., when it includes many waves with random phases.²³ This condition though is well satisfied in the strong turbulence cases studied here. For a R/L_T scan based on the GA-standard case, computed using GYRO, it was seen that $K < 1$.⁴ This was done calculating the autocorrelation time as $\tau_{ac} = 2D/\langle |v_x|^2 \rangle$, where D is the particle diffusivity, as carried out in Ref. 24. This assumes a priori that the particle transport is due to a random-walk process in the oscillating field. In this work, we calculate the Kubo number by a more direct method, by calculating the τ_{ac} directly from the fluctuating potential field from GENE non-linear simulations. The time correlation function is $C(\Delta t) = \langle \phi(x, y, t)\phi(x, y, t + \Delta t) \rangle / \langle |\phi|^2 \rangle$, averaging over the x and y directions. The parallel coordinate is kept fixed at the low-field side. The correlation time is taken as the $1/e$ time of this function. All $n = 0$ modes are not included in the calculation, which thus considers only the flux inducing $n > 0$ background drift-wave population. λ_x is calculated as the $1/e$ length of the function $C(\Delta x) = \langle \phi(x, 0, t)\phi(x + \Delta x, 0, t) \rangle / \langle |\phi|^2 \rangle$. $\langle v_x \rangle = \sqrt{\langle E_y^2 \rangle} / B_{ref}$, with the same averaging procedure as τ_{ac} for consistency. B_{ref} is the reference magnetic field used to normalize the GENE equations and variables.

We have calculated the Kubo numbers for the full set of GENE non-linear runs. The calculated correlation lengths,

TABLE II. Grid settings and results of converged GENE non-linear runs.

Run	n_x	n_y	k_{ymin}	n_z	n_v	n_w	L_x	Sim time [R/c_s]	$\chi_i/\chi_e/D$ [GB units]
A: $s = 1$	140	16	0.05	16	32	8	100	950	39.64/9/-0.75
A: $s = 0.6$	140	16	0.05	16	48	8	140	960	39.94/13.21/0.26
A: $s = 0.1$	256	24	0.05	16	48	8	200	560	21.84/11.51/2.57
A: $s = -0.4$	256	25	0.03	16	32	8	166	630	23.66/11.67/5.36
B: $s = 1$	140	16	0.05	16	48	8	140	800	18.33/5.7/0.9
B: $s = 0.6$	160	32	0.03	16	48	8	160	750	25.58/11.64/3.32
B: $s = 0.1$	300	32	0.03	16	48	8	333	720	11.63/7.88/2.84
B: $s = -0.4$	160	32	0.03	16	48	8	160	640	13.37/9.62/3.86
C: $s = 1$	140	16	0.05	16	48	8	140	1570	9.54/1.77/-0.01
C: $s = 0.6$	210	24	0.05	16	48	8	140	600	17.65/5.22/0.95
C: $s = 0.1$	300	32	0.03	16	48	8	200	600	7.74/4.01/1.29
C: $s = -0.4$	240	24	0.05	16	48	8	160	610	7.32/4.89/1.9
D: $s = 1$	200	32	0.05	16	48	8	200	610	8.94/2.25/0.05
D: $s = 0.6$	240	32	0.05	16	48	8	160	385	15.69/6.08/1.46
D: $s = 0.1$	300	32	0.05	16	48	8	200	560	9.18/5.42/1.87
D: $s = -0.4$	240	32	0.05	16	48	8	160	380	7.87/5.61/2.2

TABLE III. Correlation times, lengths, and Kubo numbers for the GENE non-linear runs. Units are Larmor radii for the lengths, and R/c_s for the times.

Run	$\sqrt{\langle E_y^2 \rangle}$	λ_x	t_{ac}	K
A: $s = 1$	8.6	12.60	1.85	0.42
A: $s = 0.6$	11.78	11.2	2.05	0.72
A: $s = 0.1$	12.23	7.12	0.58	0.33
A: $s = -0.4$	9.66	6.94	1.85	0.86
B: $s = 1$	8.7	12.70	2.14	0.49
B: $s = 0.6$	10.8	10.50	1.74	0.60
B: $s = 0.1$	8.59	6.90	1.09	0.45
B: $s = -0.4$	7.93	6.87	2.14	0.82
C: $s = 1$	5.37	13.67	1.90	0.27
C: $s = 0.6$	8.48	10.92	3.44	0.89
C: $s = 0.1$	6.69	7.30	1.44	0.44
C: $s = -0.4$	5.5	6.08	2.01	0.61
D: $s=1$	7.38	9.76	0.96	0.24
D: $s = 0.6$	9.23	8.41	1.38	0.50
D: $s = 0.1$	7.67	5.88	1.20	0.52
D: $s = -0.4$	6.9	5.93	1.96	0.76

times, and Kubo numbers can be found in Table III. For all cases, $K < 1$. We thus conclude that the quasilinear approximation indeed holds. Note furthermore that $K < 1$, but still of order unity, supports the application of the mixing length rule for setting the level of the saturated potential, where the implicit assumption is that the step length of the random walk process is the eddy size. While the quasilinear approximation itself may hold, the value of the saturated electrostatic potential cannot be determined by linear theory. This value is determined by a mixing length rule, whose validation at low magnetic shear is evaluated in the Sec. IV C.

C. Reevaluation of the QuaLiKiz saturated potential model

The model for the saturated potential is comprised of three parts: the model for k_\perp , setting the k_y maximum and spectral shape of the non-linear flux spectrum, and frequency broadening. We briefly recall here the previous model. The k_y maximum of the flux spectrum is designated $k_y|_{max}$ and corresponds to the maximum of the mixing-length flux spectrum $\frac{\gamma_k}{\langle k_x^2 \rangle}$,^{12,25} where

$$\langle k_\perp^2 \rangle = k_y^2 \left(1 + (s - \alpha)^2 \langle \theta^2 \rangle \right). \quad (4)$$

This formulation of k_\perp calculates only the effective k_x due to the shearing of the mode along the field line and assumes that the dominant instability has intrinsic $k_x = 0$.

The k-spectrum is k_y^{-3} and k_y^3 above and below the flux spectrum maximum, respectively. The frequency spectrum of the saturated potential is broadened by the linear growth rate as follows: $\phi_k(\omega) \propto \frac{\gamma_k}{(\omega - \omega_k)^2 + \gamma_k^2}$. This model has been shown to lead to discrepancies both in the k_y of the saturated potential peak and in the frequency spectrum width when compared to GENE non-linear results at low magnetic

shear. The k-spectrum model is reviewed and an improved formulation for k_\perp is proposed in Sec. IV C 1. The frequency spectrum broadening comparison and consequences of the discrepancy are addressed in Sec. IV C 2.

1. Choice of k_\perp and the model for calculating the flux spectrum peak

The correlation length of the turbulence is set both by the k_x inherent in the k_\perp formulation and also by $k_y|_{max}$. The magnetic shear dependence in Eq. (4) suggests (with $\alpha = 0$) that the effective k_x is lower at $s = 0.1$ than at $s = 1$ (for the same $k_y|_{max}$). This would correspond to increased correlation lengths as the magnetic shear is reduced. The k_x and k_y components of k_\perp from Eq. (4) are plotted in Figure 5, for the GA-standard $s = 1$ and $s = 0.1$ case, where $\langle \theta^2 \rangle$ is calculated from the QuaLiKiz eigenmode ansatz. At $s = 1$, the assumed structures are approximately isotropic, particularly at lower, transport relevant k_y . At $s = 0.1$, $k_x < k_y$. Even though $\langle \theta^2 \rangle$ increases as the magnetic shear decreases, this does not compensate the decreasing s^2 , at least down to $s = 0.1$. This was corroborated by linear GENE analysis, where the eigenmodes were self-consistently calculated.

However, the magnetic shear dependence in Eq. (4) is not consistent with the non-linear results, where the correlation length decreases with decreasing magnetic shear, as seen in Table III. The eddy structure for both the $s = 0.1$ and $s = 1$ non-linear GA-standard cases are shown in Figure 6. The structures are roughly isotropic. The decreased correlation length at low magnetic shear is a result of the increased $k_y|_{max}$ at $s = 0.1$.

Therefore, the $k_y|_{max}$ calculation is also critical for setting correlation length and flux values. However, it was found that due to the large weight of $1/k_y^2$ at low k_y , $k_y|_{max}$ typically corresponds to the lowest (in k_y) unstable mode, in spite of the relatively low growth rates. For QuaLiKiz, this is typically in the range of $k_y = 0.05 - 0.1$. This is in disagreement with the non-linear flux spectra maxima from the magnetic shear scans, only agreeing approximately at $s = 1$. Thus both the k_\perp and $k_y|_{max}$ formulations must be rectified to correctly account for the magnetic shear dependencies on the flux in the mixing length model.

The non-linear flux spectra maxima, $k_y|_{max}$, were reproduced by replacing the effective k_x in k_\perp with the actual k_x values from the non-linear simulations. Thus, $k_\perp^2(nl) = k_y^2 + \langle k_x \rangle_{nl}^2(k_y)$, where $\langle k_x \rangle_{nl}(k_y)$ is the averaged value of k_x for each k_y mode in the non-linear simulation. $\langle k_x \rangle(k_y)$ is defined as $\sum k_x |\phi(k_x, k_y)|^2 / \sum |\phi(k_x, k_y)|^2$, where the summation is over $k_x \geq 0$ for a given k_y . The values of $|\phi(k_x, k_y)|^2$ are pairwise averaged over negative and positive k_x , as well as over the parallel coordinate and for the times corresponding to the saturated state of the simulation. In the non-rotating, up-down symmetric plasmas considered in our simulations, k_x is symmetric around 0. In Figure 7, these $\langle k_x \rangle$ values are plotted versus k_y for the GENE non-linear GA-standard case magnetic shear scan. At low k_y , the eddies are not isotropic. $\langle k_x \rangle$ does not continue to drop at low k_y , and saturates at a value which increases as the magnetic shear decreases. This corresponds to reduced correlation lengths at low magnetic shear.

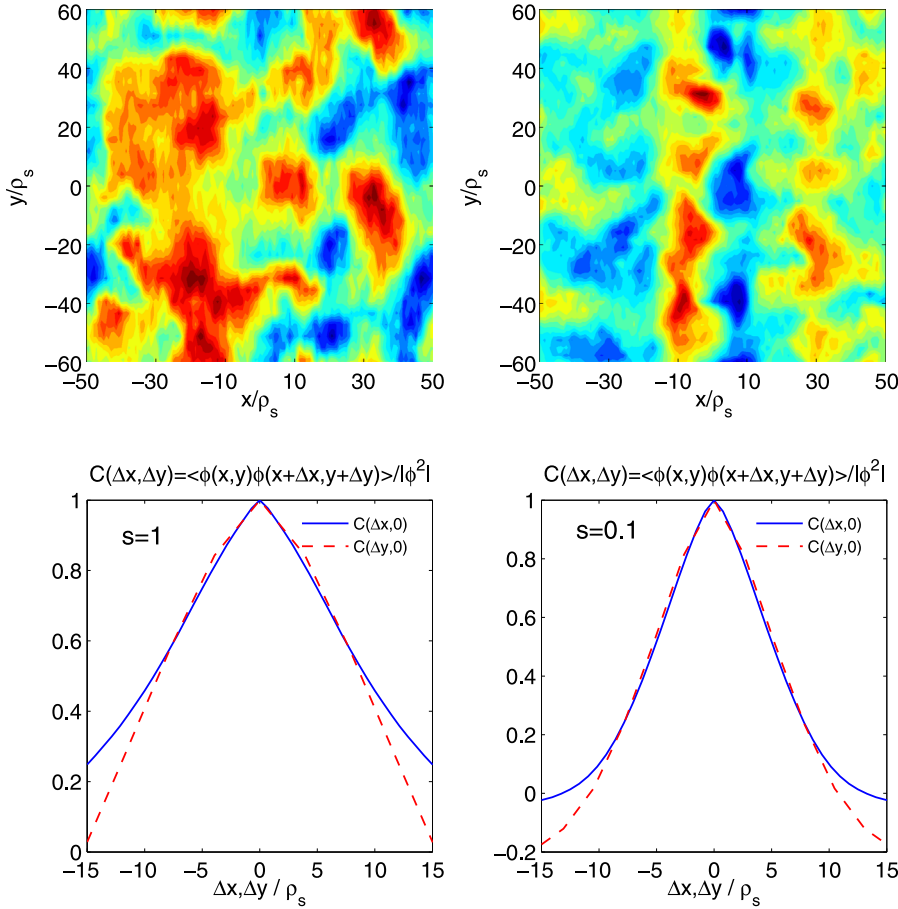


FIG. 6. Contours of the electrostatic potential (top row) and the x and y length correlation functions (bottom row) for a typical timeslice in GENE $s = 1$ (left column) and $s = 0.1$ (right column) GA-standard case simulations.

The $k_y|_{max}$ corresponding to the maximum $\gamma_k/k_\perp^2(nl)$ corresponds well with the non-linear flux spectra k_y maximum, as seen in Figure 8 for the entire range of non-linear simulations carried out. γ_k was taken from GENE linear simulations and $k_\perp^2(nl)$ from GENE non-linear simulations. The considerations raised in Sec. III A—the stabilization of the toroidal branch at low sk_y —also plays a role in setting $k_y|_{max}$. Not only is $\langle k_x \rangle$ increased at low magnetic shear, but the growth rates themselves are reduced at low sk_y , further increasing the obtained $k_y|_{max}$, leading to reduced correlation lengths at low magnetic shear.

In light of these observations from the non-linear simulations, we have improved the k_\perp^2 formulation in QuaLiKiz by taking into account the non-linear contribution to $\langle k_x \rangle$. This simultaneously recovers the non-linear flux spectra k_y maximum and provides the magnetic shear and q-profile dependence on the precise relation between k_y and $\langle k_x \rangle$ at $k_y|_{max}$. We have found that the following relation successfully reproduces the non-linear $\langle k_x \rangle(k_y)$ for the magnetic shear and q-profile scans carried out in this work:

$$\langle k_x \rangle(k_y) = k_y s \sqrt{\langle \theta^2 \rangle} + 0.4 \frac{e^{-2|s|}}{\sqrt{q}} + \frac{3}{2} (k_y - 0.2) H(k_y - 0.2), \quad (5)$$

where H is a Heaviside function. The first term on the RHS is the effective k_x due to the magnetic shear, which also appears in the previous k_\perp^2 formulation. The second term approximates the value of the non-linear contribution to $\langle k_x \rangle$

in the long wavelength, transport relevant region. The third term on the RHS was set to fit the non-linear $\langle k_x \rangle$ at higher k_y , and only plays a minor role at transport relevant k_y . The first term dominates at high magnetic shear, while the second term dominates at low magnetic shear. The QuaLiKiz mixing length rule formulation for k_\perp^2 was thus set in accordance with Eq. (5). The results for $k_y|_{max}$, using the QuaLiKiz γ_k and the new $k_\perp^2 = k_y^2 + \langle k_x \rangle^2$, are seen in Figure 9, where the results for the newly formulated k_\perp^2 are compared with the previously formulated k_\perp^2 . The new formulation leads to a much improved reproduction of the non-linear $k_y|_{max}$. The absolute value $|s|$ in the exponent in the $\langle k_x \rangle$ formulation was set to avoid a non-physical exponential increase of $\langle k_x \rangle$ at

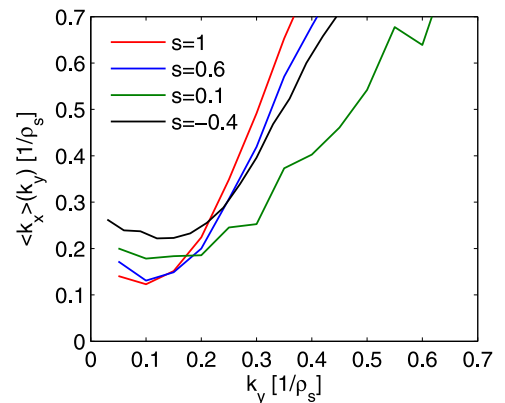


FIG. 7. $\langle k_x \rangle(k_y)$ for the k_y points from a GENE non-linear GA-standard magnetic shear scan.

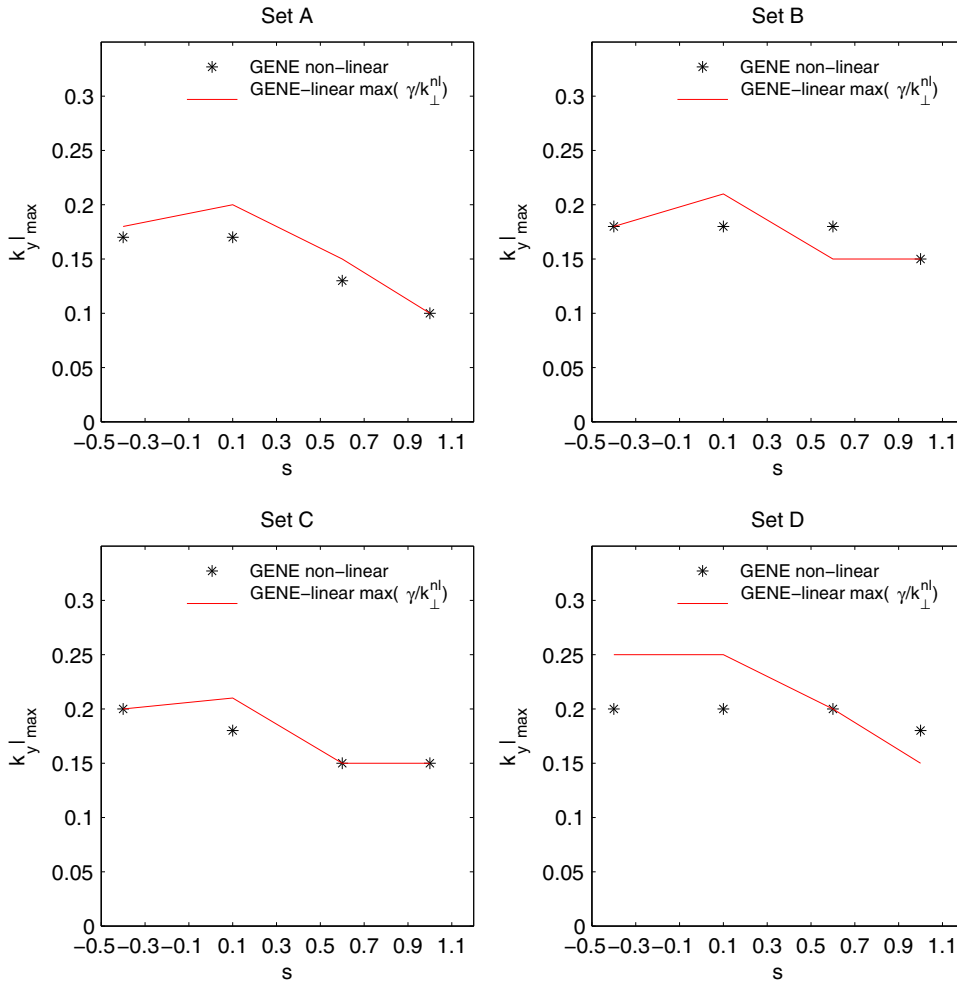


FIG. 8. Comparison of $k_y|_{max}$ from non-linear simulations, and from the maximum of the $\gamma_k/k_{\perp}^2(nl)$ spectrum, where γ_k is from GENE-linear calculations, and $k_{\perp}^2(nl) = k_y^2 + \langle k_x \rangle^2(k_y)$ is taken from the non-linear simulations.

large absolute values of negative magnetic shear. While the continuing decrease of the correlation length at negative magnetic shear is then not captured, we note that in general, the QuaLiKiz predictions at negative magnetic shear deviate from the non-linear predictions due to an underprediction of the slab ITG branch. This is seen in Figure 9, for $s < \sim -0.3$, where the high values predicted for $k_y|_{max}$ is due to mode stabilization at lower k_y , and not due to k_{\perp}^2 . The present formulation is thus relevant for low magnetic shear, while improved agreement between QuaLiKiz and non-linear flux predictions at negative magnetic shear is left for future work.

In addition to improving the k_{\perp} formulation, we can consider also introducing a shearing effect of zonal flows on large wavelength turbulence.²⁶ This can be done by a ExB quench rule similar to that employed in the gyro-Landau-fluid and trapped gyro-Landau-fluid models GLF23 (Refs. 27 and 28) and TGLF (Ref. 29) for external toroidal velocity. Indeed, the non-linear $k_y|_{max}$ was also recovered by calculating $\max(\gamma_{eff}/k_y^2)$, where γ_{eff} is a quenched growth rate taken as $\gamma_{eff} = \max(0, \gamma_k - 0.3\omega_{ExB})$. ω_{ExB} is the effective zonal flow ExB shear rate taken from the GENE non-linear simulations, including the effect of the autocorrelation time on the effective shearing time.³⁰ 0.3 is a tuned coefficient, which provided a best fit to the non-linear flux spectra maxima throughout the set of simulations. k_{\perp} was replaced by k_y due to the approximate k_x and k_y isotropy. However, the simultaneous inclusion of γ_{eff} and the improved k_{\perp} formulation does

not change the calculation of $k_y|_{max}$ compared to the sole inclusion of the improved k_{\perp} formulation. This is because the role played by the zonal flow shearing—the quenching of long wavelength modes—is effectively played by the non-isotropy of k_y and k_x at low k_y . Due to the challenge in parameterizing the zonal flow shear rate ω_{ExB} throughout parameter space within QuaLiKiz and given the minor effect the zonal flow shearing of low k_y modes has on determining $k_y|_{max}$ if the non-linear $\langle k_x \rangle$ is included in the model, it was decided not to include a zonal flow growth rate quench model in QuaLiKiz.

A possible mechanism for the dependence of magnetic shear on the zonal flow impact on $\langle k_x \rangle$ is now discussed. In non-linear mode coupling, the amount of energy that is injected into the primary mode is balanced by the coupling to other modes at the same scale or nearby scales. In general, this coupling must satisfy a frequency matching condition as well as a wavenumber matching condition ($\omega_p + \omega_q - \omega_k = 0$, $\mathbf{p} + \mathbf{q} - \mathbf{k} = 0$). At high magnetic shear, the modes are more strongly ballooned (more localized around $\theta = 0$); and in addition, the effective local radial wavenumber varies poloidally, since $k_x^{eff} \sim k_y \hat{s} \theta + k_x$. This makes it rather difficult for the dominant ballooning eigenmode to couple effectively to a zonal mode, which is poloidally symmetric, with a direct interaction. However, in the case of low shear, the ballooning structure of the primary mode is much less pronounced; and in addition, the local k_x^{eff} is a much weaker function of θ . This

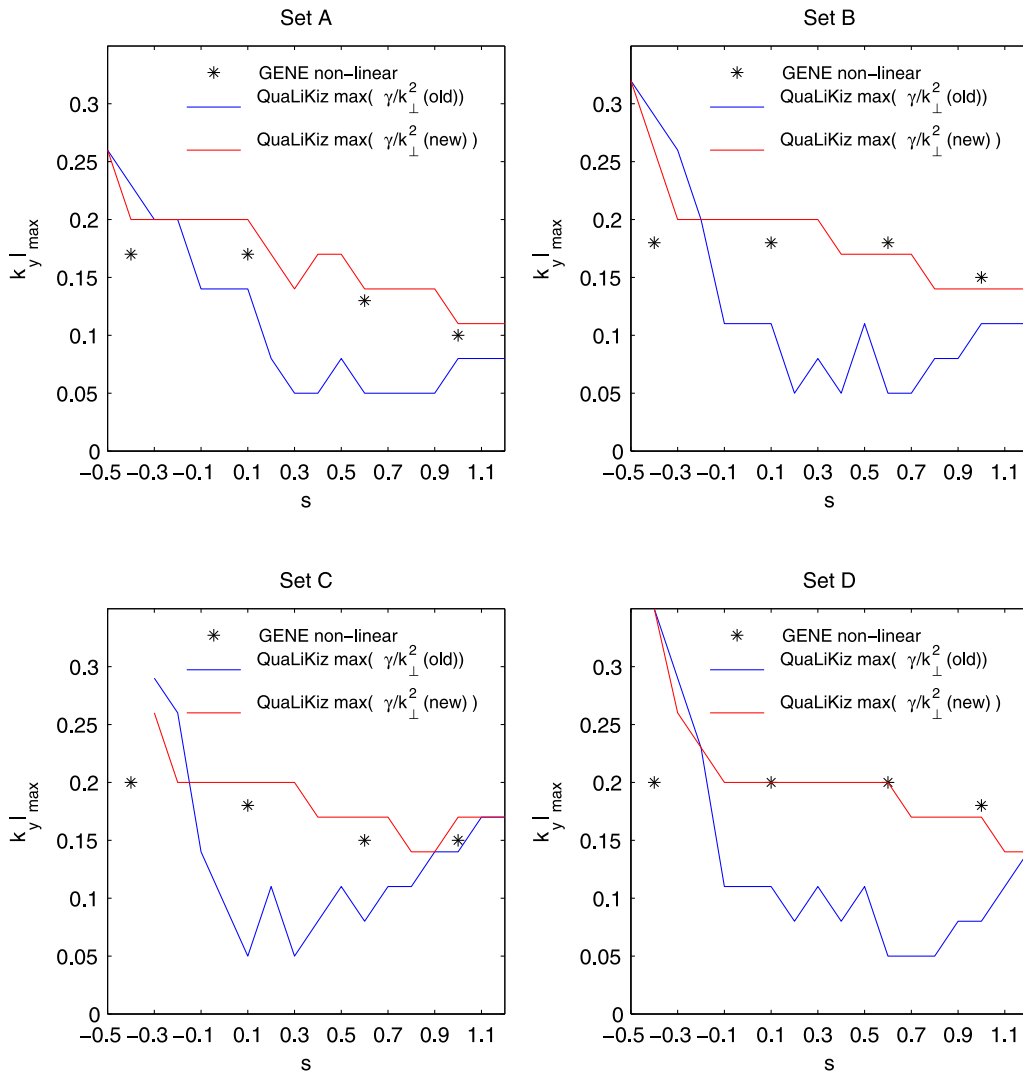


FIG. 9. Reproduction of the non-linear flux spectra maximum from the maximum of the $\gamma_k/k_{\perp}^2(nl)$ spectrum, where γ_k is from QuaLiKiz, and $\langle k_x \rangle^2$ is taken from a formula found to reproduce the values predicted by GENE non-linear simulations.

makes it easier for the primary mode to couple directly to a zonal mode. This dependency of magnetic shear on zonal flows is well known and has been observed in a number of different contexts, for example, in ETG gyrofluid simulations.³¹ In the direct simulations carried out in this work, the relative amplitude of zonal flows is indeed found to be greater at low magnetic shear, as seen in Figure 10 for the set A (GA-standard case) $s = 1$ and $s = 0.1$ cases. The saturated electrostatic potential amplitudes are normalized, thus the lower normalized amplitude of the $s = 0.1$ $k_y > 0$ spectrum compared to the $s = 1$ case reflects the higher relative amplitude of the $s = 0.1$ $k_y = 0$ modes (zonal flows) compared with the $s = 1$ case.

Since in the case of wave interactions, it takes at least three waves to interact, when the direct interaction with the zonal flow is allowed, another drift mode with non-zero k_x also extracts energy from this interaction (in fact enstrophy and not energy is exchanged, but for the sake of current argument, this is not of essential importance). This has two effects on turbulence. First, the zonal flows isotropize turbulence, since they can shear streamers apart. They also reduce the degree of ballooning in the mode structure. This isotropization

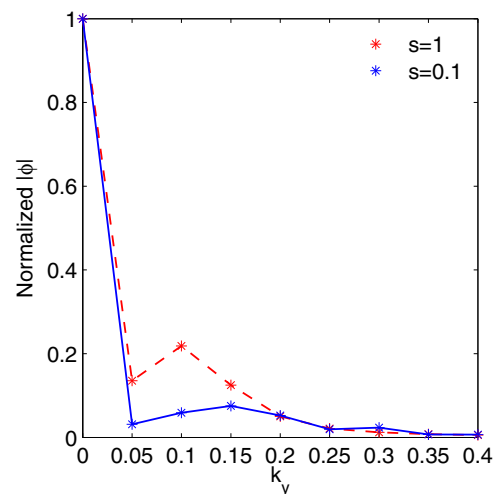


FIG. 10. Relative amplitude of zonal flow modes ($k_y = 0$) compared with the $k_y > 0$ modes for the GA-standard $s = 1$ and $s = 0.1$ cases. k_x has been averaged over at each k_y .

can make the non-linearly formed k_x important in the computation of the flux or the mixing length saturation level. At high magnetic shear, the ‘non-linear’ k_x is less important, since the zonal flow drive is lessened due to effective k_x being a function of θ . But at low magnetic shear, the turbulence is isotropized due to zonal flows, so a substantial amount of the energy is found in $k_x \neq 0$ fluctuations.

In summary, the previous k_{\perp}^2 formulation in QuaLiKiz led both to an incorrect estimate of the non-linear flux spectrum maximum and to the wrong dependency on magnetic shear in the k_{\perp}^2 description itself at low magnetic shear. From analysis with non-linear and linear GENE simulations, it was found that improving the k_{\perp}^2 formulation in the QuaLiKiz mixing length rule, taking into account the $\langle k_x \rangle(k_y)$ found from non-linear simulations, leads to an improved estimate of $k_{y|max}$ and the magnetic shear and q-profile dependence of k_{\perp}^2 . The increased values of $\langle k_x \rangle(k_y)$ at low magnetic shear at low, transport relevant, k_y values may be related to the observed greater relative amplitude of zonal flow modes. This may rise due to the less pronounced ballooning structure of the low magnetic shear eigenmodes. It is also possible that linearly unstable modes with k_x -center $\neq 0$ —which are more prevalent at low magnetic shear—further contribute to the k_x spectrum.

2. Frequency broadening

In the QuaLiKiz model, the width of the broadened electrostatic field frequency function due to stochastic scattering is taken as the linear growth-rate, γ_k . This assumption can be checked by comparison to the non-linear frequency spectra from GENE. The width of the non-linear frequency spectra, calculated for each k_y , is compared to the linear growth rate from linear GENE. In Figure 11, we see the examples of the frequency broadening data and Lorentzian fit from set A (GA-standard case) $s = 1$ and $s = 0.1$ cases for $k_y = 0.2$. The GENE calculated linear frequency (ω_{lin}) and growth rate (γ_{lin}) are compared with the non-linear frequency spectrum center (ω_{fit}) and width ($\Delta\omega_{fit}$) as defined by the Lorentzian fit. We

note that in analysis of GYRO frequency spectra, both Lorentzian and Gaussian fits to the frequency spectra were satisfactory in recovering the FWHM, while a T-model was in fact the best fit to the data.¹⁰ In Figure 12, the comparison between the non-linear frequency spectra width (from the Lorentzian fit) and the linear growth rate is shown for all the sets at $s = 1$, $s = 0.6$, and $s = 0.1$. The assumption generally holds for $s = 1$ and $s = 0.6$ in the transport-relevant range of $k_y < 0.3$. However, it is very interesting to note that for $s = 0.1$, the frequency width does not equal the linear growth rate for any value of k_y . In the transport relevant range $0.15 < k_y < 0.5$, the non-linear frequency width is significantly higher than the linear growth rate estimation. This is consistent with the generally lower autocorrelation times observed at low magnetic shear, as seen in Table III. This must be taken into consideration in the quasi-linear model.

This increased frequency broadening at low magnetic shear may be a result of non-linear decorrelation mechanisms, such as zonal flows, which play a stronger role at low magnetic shear as discussed in Sec. IV C 1. Also in the set with lowest flux, set D, where the impact of zonal flows is also expected to be stronger due to the vicinity to the instability threshold, the frequency broadening is greater than the linear growth rate estimation even at $s = 0.6$ and $s = 1$. The existence of zonal flows affects the response function. This can be seen via a renormalization of the wave-kinetic equation. In the presence of zonal flows, the basic wave-kinetic response function takes the form

$$R = \frac{R_0}{\left[1 + R_0^2 \left(\frac{\partial}{\partial r} [V_E(r)k_y] \right)^2 \frac{1}{N} \frac{\partial^2 N}{\partial k_x^2} \right]},$$

where N is the wave action. Using this form instead of the linear response function, we obtain

$$|\Phi_{k,\omega}|^2 \propto \frac{|\Phi_k|^2}{(\omega - \omega_k)^2 + \gamma_k^2 + \alpha \left(\frac{\partial}{\partial r} V_E(r) \right)^2},$$

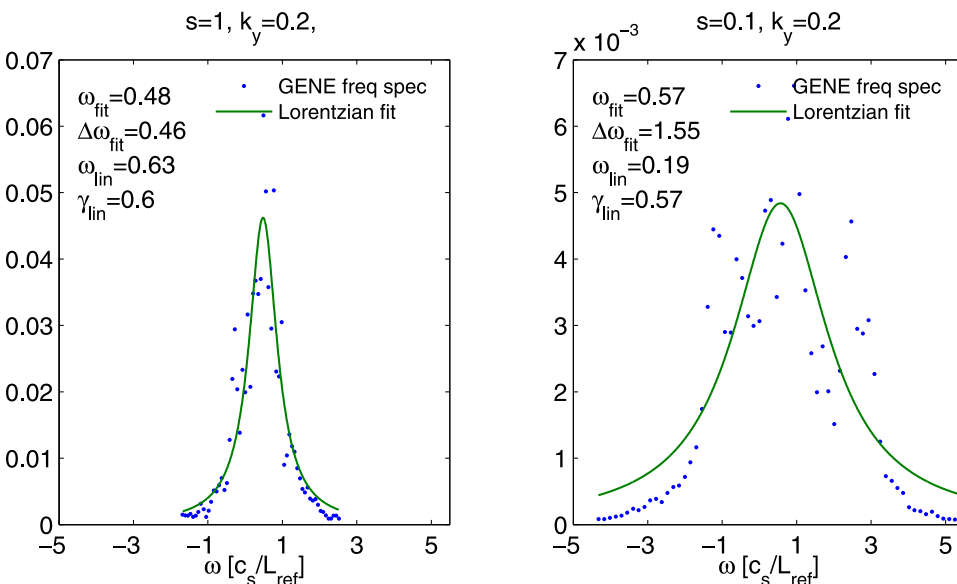


FIG. 11. Frequency spectra for $k_y = 0.2$, averaged over saturated periods of GENE non-linear simulations from set A with $s = 1$ (left panel) and $s = 0.1$ (right panel).

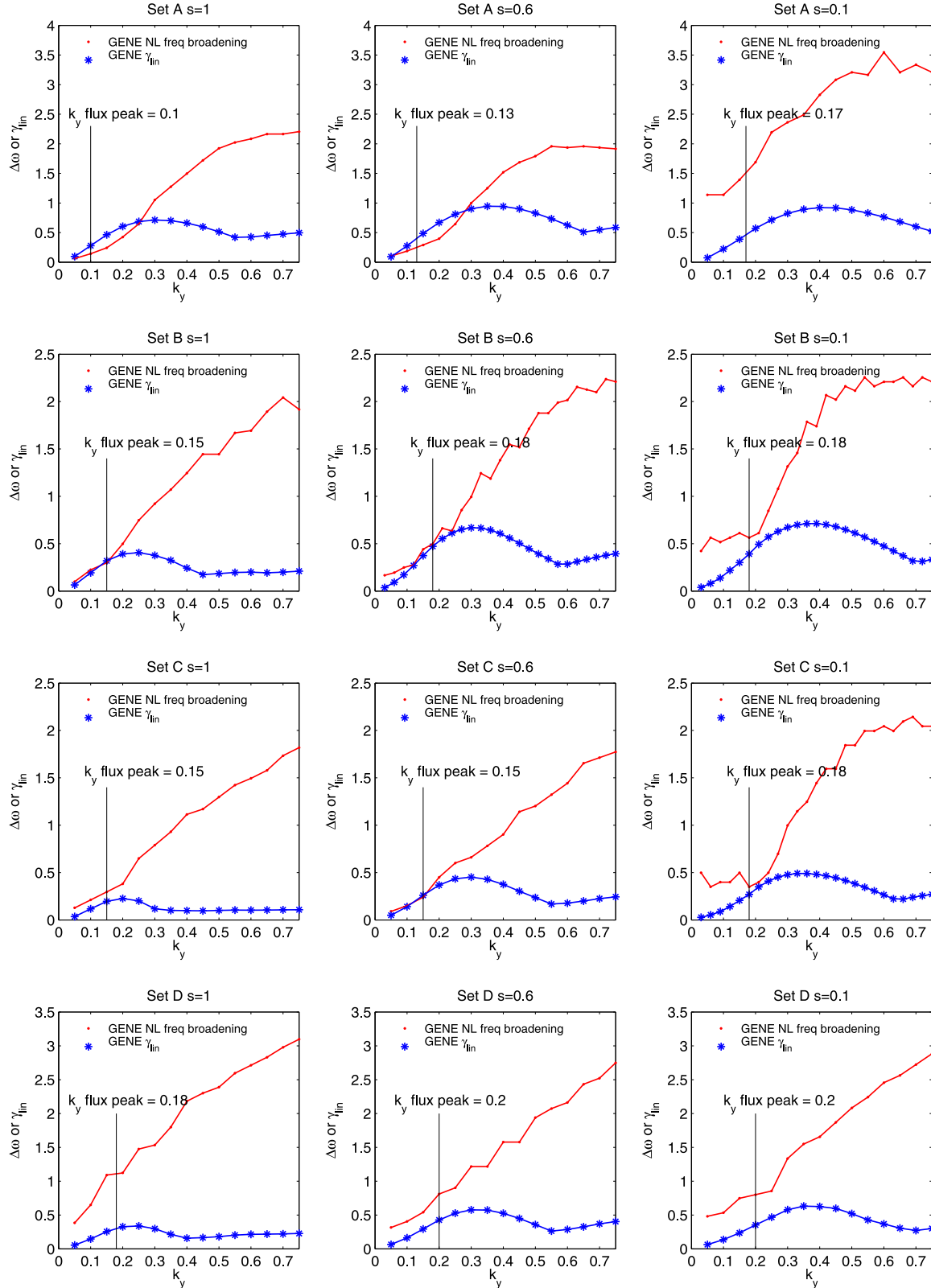


FIG. 12. Non-linear frequency spectra fitted Lorentzian width and linear growth rates are compared for a range of k_y , for all 4 sets studied, for $s = 1$ (left column), $s = 0.6$ (middle column), and $s = 0.1$ (right column).

where $V_E(r)$ is the zonal flow velocity, and $\alpha \equiv \frac{k_y^2}{|\Phi_k|^2} \frac{\partial^2 |\Phi_k|^2}{\partial k_x^2}$. This equates to increased frequency broadening, beyond the linear growth rate assumption. Such a reduction of the fluxes due to perpendicular flow shear was also employed in a transport model by Hinton and Staebler.³²

We define the ratio between the frequency broadening from the non-linear simulations and the linear growth rate, at each magnetic shear value, as the weighted average $\langle \Delta\omega_k / \gamma_k \rangle$, with the weight set by the $\phi(k_y)$ amplitude spectrum. For the entire collection of simulations, $\langle \Delta\omega_k / \gamma_k \rangle_{s=0.1} / (\frac{1}{2} \langle \Delta\omega_k / \gamma_k \rangle_{s=1})$

$+\frac{1}{2}\langle\Delta\omega_k/\gamma_k\rangle_{s=0.6}) = 2.5$, averaging over all four sets. This reflects the increased frequency broadening at low magnetic shear, which is highest for set A (GA-standard case) and lowest for set D. In the absence of more rigorous theory, we have simply included an additional shear dependent normalization factor to the fluxes calculated by QuaLiKiz, in the form of $2.5(1 - |s|)$ for $|s| < 0.6$. This normalization factor roughly captures the effect of the decreased autocorrelation time due to increased frequency broadening (possibly due to zonal flows) at low magnetic shear.

The increase in the frequency broadening is also correlated with a reduction in the effective non-linear transport weight. This is seen by comparing the ratio of the quasilinear transport weight (flux over spectral intensity as a function of k) with the non-linear transport weight, defined as an *average*.³³ These averages were found to be ~ 1.4 —at transport relevant k values—for a variety of different cases. When calculating this average for the $s = 0.1$ GA-standard case, as seen in Figure 13, we however obtain an increased average compared to the ~ 1.4 value found for the $s = 1$ case. This average increase, corresponding to the deviation of the quasilinear flux from the non-linear flux due to the non-constancy of the transport weight, corresponds well with our *ad-hoc* correction factor from the frequency broadening.

An additional possible explanation for the non-unity average could be the non-linear transfer of energy from unstable eigenmodes to stable eigenmodes. This is proposed to lead to a similar factor ~ 1.4 between quasilinear and non-linear fluxes.³⁴ This is because the construction of the quasilinear flux assumes that the unstable mode contributes fully to the electrostatic potential amplitude. However, in the non-linear case, linearly damped modes take up a given proportion of the total electrostatic potential amplitude. The net contribution of these linearly damped modes to the flux is typically much reduced compared with the dominant unstable mode. Thus, since the transport weight (following a k_y decomposition) is defined as the flux divided by the electrostatic potential, the non-linear weight is expected to be lower than the quasilinear weight due to the existence of the

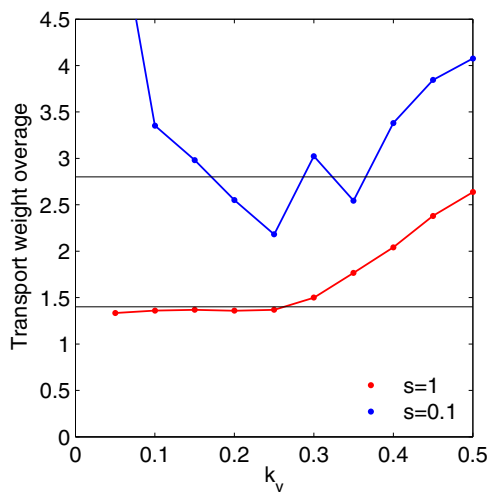


FIG. 13. Ratio of quasilinear to non-linear transport weights for the GA-standard $s = 1$ and $s = 0.1$ cases.

low-flux-contributing linearly damped modes, which do contribute to the saturated electrostatic potential amplitude. An increased proportion of linearly damped modes in the low magnetic shear system would then be consistent with increased transport weight average. A broadened frequency spectrum could also be a signature of an increased spectrum of modes in the system. The increase of zonal modes—as observed at low magnetic shear—is expected to lead to increased coupling to $n > 0$ linearly damped modes. Indeed, as seen in Figure 14, singular value decompositions of the saturated electrostatic potential of the GA-standard $s = 1$ and $s = 0.1$ cases show that the $s = 0.1$ case has a much broader spectrum of linearly stable modes beyond the dominant unstable mode. This method of analysis is outlined in Hatch *et al.*³⁵ The existence of a broader spectrum of linearly damped modes is consistent with a higher transport weight average. However, we also note that at the current level of analysis, it is not possible to separate in the singular value decomposition linearly damped modes from linearly unstable modes with midplane $k_{x0} \neq 0$ (related to the conventional ballooning angle through $k_{x0} = k_y \theta_0 s$). While the $k_{x0} = 0$ modes are dominant for both $s = 0.1$ and $s = 1$, the k_{x0} growth rate spectrum is broader for $s = 0.1$, when compared with $s = 1$. These modes could in principle also contribute to the frequency broadening. More analysis is necessary in this respect.

In summary, at low magnetic shear, the non-linear frequency broadening is observed to be larger than the linear growth rate width assumption. This broadening is correlated with an increase in the quasilinear to non-linear transport weight average. An *ad-hoc* magnetic shear dependent normalization factor, based on the degree of increased non-linear frequency broadening at low magnetic shear, has been introduced into QuaLiKiz. The physical explanation of the frequency broadening and associated transport weight average increase may be related to the relative increase in the zonal flow amplitude at low magnetic shear. A direct renormalization of the linear response function due to zonal flows is suggested. An additional explanation may be the increased non-linear coupling (via zonal flows) to linearly

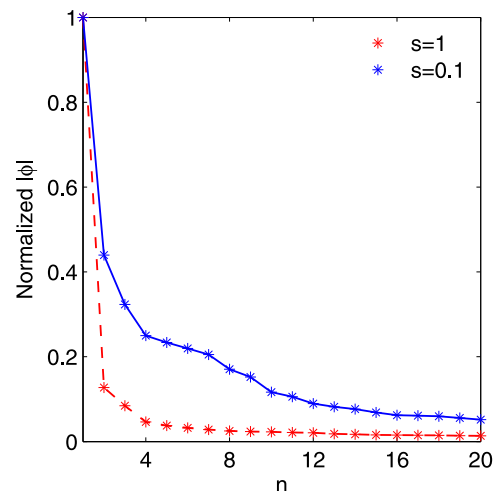


FIG. 14. Singular value spectrum of mode amplitudes calculated from the GA-standard $s = 1$ and $s = 0.1$ saturated electrostatic potentials.

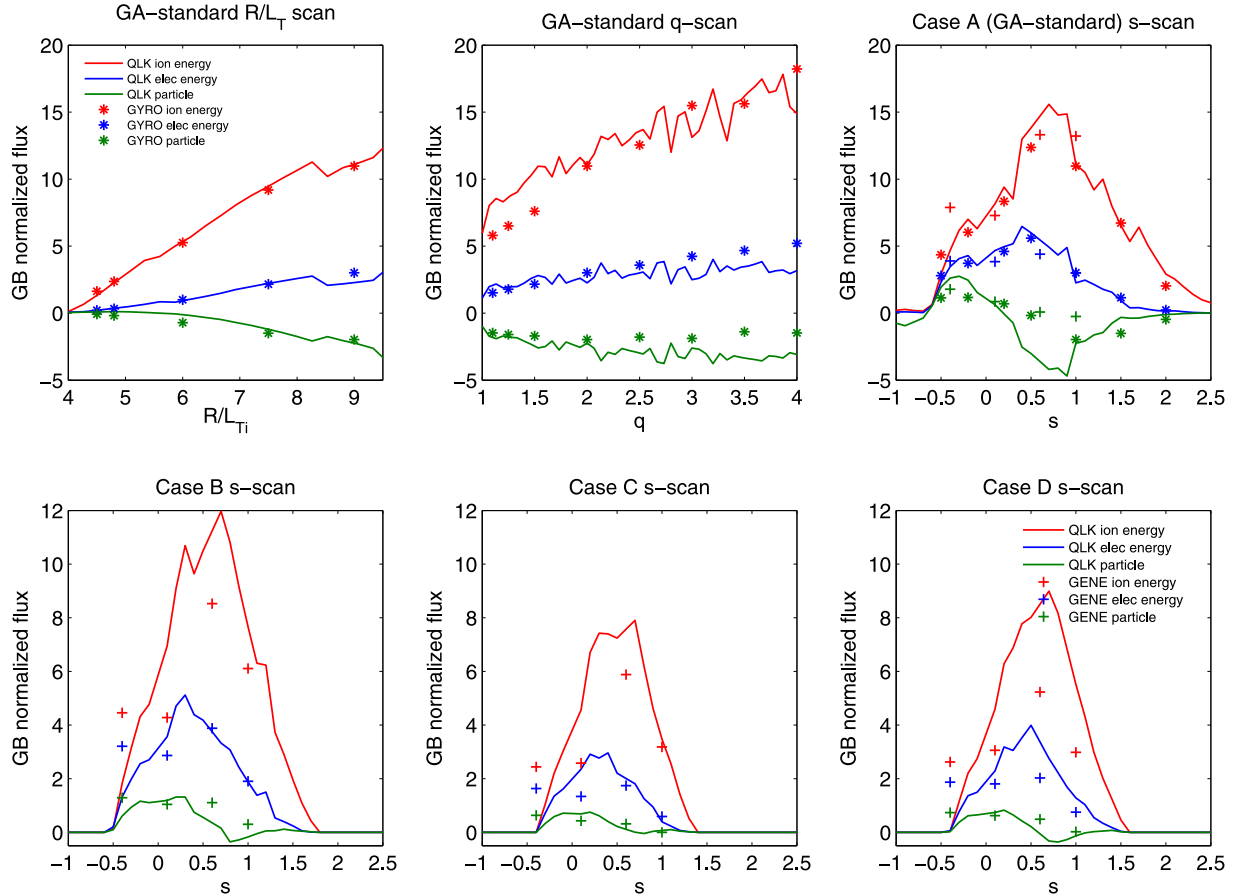


FIG. 15. Comparison of the altered QuaLiKiz model with the 4 sets of GENE runs, and with the GYRO GA-standard case s-scan, q-scan, and R/L_T scan.

damped modes. More theoretical work is necessary to more fully uncover the mechanism of the increased frequency broadening and transport weight overage increase at low magnetic shear. However, on a more pragmatic level, the QuaLiKiz and non-linear flux prediction comparison is much improved through the combination of the k_{\perp} formulation improvement and the *ad-hoc* magnetic shear dependent normalization. This is shown in Sec. IV D.

D. Comparison of QuaLiKiz and non-linear flux predictions

Having taken into account both modifications discussed above, the k_{\perp}^2 alteration and frequency broadening renormalization, we now compare the particle and heat flux predictions from the modified QuaLiKiz and the non-linear simulations, for all GENE runs carried out, as well as GYRO for the GA-standard magnetic shear, q-profile, and R/L_T scans. The results are displayed in Figure 15. The agreement with the GA-standard case s-scan is much improved compared to

TABLE IV. RMS errors between QuaLiKiz and non-linear simulation predicted fluxes, for all GENE and GYRO runs shown in Figure 15.

	σ_{λ_i}	σ_{λ_e}	σ_D
QuaLiKiz09	1.13	1.53	1.84
With new k_{\perp}^2 only	0.52	0.77	1.24
With new k_{\perp}^2 and frequency broadening renormalization	0.26	0.33	1

the previous mixing length formulation shown in Figure 1. Simultaneously, the agreement with the q-scan and R/L_T scan is maintained. When exploring additional areas in parameter space, i.e., the B, C, and D sets, reasonable agreement is also observed. These results are summarized in Table IV, where the RMS error between the particle and heat fluxes between QuaLiKiz and the non-linear GENE and GYRO simulations are listed. The RMS error is defined as $\sigma = \sqrt{\sum_i \epsilon_i^2 / \sum_j \chi_{j(NL)}^2}$, where ϵ_i is the diffusivity or flux difference between QuaLiKiz and the non-linear prediction for a given simulation, and $\chi_{j(NL)}$ the diffusivity or flux from the non-linear simulation. The RMS errors obtained using the previous QuaLiKiz version, correcting only k_{\perp}^2 , and both correcting k_{\perp}^2 and including the frequency broadening renormalization are all compared. Both modifications are of comparable importance.

V. DISCUSSION AND CONCLUSIONS

Quasilinear flux predictions in the previous version of QuaLiKiz did not agree with GYRO non-linear flux predictions at low magnetic shear. This work has systemically examined the assumptions underlying the QuaLiKiz model, to uncover the physics behind this discrepancy. Improvements in the model were implemented. These improvements were guided and validated by a further set of non-linear simulations carried out with GENE. This led to a significant improvement in the comparison between QuaLiKiz and non-linear simulations.

It was found that the previous formulation of k_{\perp}^2 in the QuaLiKiz mixing length rule for the saturated potential did not reproduce the magnetic shear dependence observed in non-linear simulations, neither in the $k_{y|_{max}}$ of the flux spectrum, nor in the relation between $\langle k_x \rangle$ and k_y . Furthermore, the frequency broadening at low magnetic shear was observed in the non-linear simulations to be greater than the linear growth rate broadening assumption. This is correlated with an increase in the ratio between the quasilinear and non-linear transport weights (transport weight overage), which must be taken into account in the model.

The QuaLiKiz mixing length rule was thus improved by introducing a formula for $\langle k_x \rangle(k_y)$ in the k_{\perp} formulation, which captures the magnetic shear and q-profile dependence from the non-linear simulations. This successfully reproduces the non-linear $k_{y|_{max}}$ from the maximum of the γ_k/k_{\perp}^2 mixing length spectrum and also captures the degree of isotropy between $\langle k_x \rangle$ and k_y , setting the precise value of the correlation length. Furthermore, a renormalization based on the weighted average of the increased frequency broadening was implemented, which was consistent with the observed degree of increase in the transport weight overage. These modifications led to a much improved agreement between the new version of QuaLiKiz and non-linear GYRO and GENE magnetic shear scans for various values of R/L_T , q , and T_i/T_e .

We note that the reproduction of $k_{y|_{max}}$ can also be achieved by invoking zonal flow quenching of large wavelength turbulence in the mixing length rule. This results in reduced correlation lengths at low magnetic shear due to the stabilization of the toroidal ITG branch at combined low s and k_y , which leads to reduced growth rates at low sk_y . This stabilization was discussed when summarizing linear analytical and numerical results at low magnetic shear. In spite of the lower ITG threshold at low magnetic shear, the γ -stiffness is also lower at low magnetic shear. At low k_y , this is particularly the case, due to toroidal ITG branch stabilization at low sk_y . Since the $\langle k_x \rangle$ dependence on k_y also depends on zonal flows, these two approaches for altering the mixing length rule stem from the same physics.

As detailed in Appendices B and C, the intrinsic assumptions in the QuaLiKiz model were also examined. It was found that locality holds down to $s = 0.1$. The lowest order ballooning representation is also valid down to $s = 0.1$, following comparisons of the QuaLiKiz fluid eigenmode assumption and GENE linear eigenfunction solutions. The quasilinear approximation also holds at low magnetic shear. This was verified by calculating the Kubo numbers from the entire set of non-linear GENE simulations. It was found the $K < 1$ also at low magnetic shear. This strengthens the claim that the quasilinear/non-linear discrepancy at low magnetic shear is purely due to the formulation of the saturated potential intensity and frequency spectrum—which is outside of the scope of the quasilinear model itself—while the fundamental formulation of quasilinear diffusivities is still valid.

Future work on QuaLiKiz will be directed on reproducing the effect of external ExB shear and introducing a parameterization for shape effects beyond the $s - \alpha$ model. Furthermore, from the magnetic shear scans, we can see that ITG-TEM modes are fully stabilized at high magnetic shear.

These correspond to experimentally relevant values towards the edges of tokamak plasmas. This is not consistent with density fluctuation measurements, which increase strongly with r/a . Present quasilinear models based purely on ITG-TEM-ETG modes tend thus to underpredict the level of transport towards the edge, compared to experimental measurements, if not constrained to a typical range of $r/a < \sim 0.8$. Resolving this issue is critical for fully predictive modeling of L-modes up to the separatrix or for the region close to an H-mode pedestal.

Finally, the improved agreement in predicted fluxes between the present version of QuaLiKiz and the non-linear simulation magnetic shear scans was not only seen in the high flux GA-standard case but also in lower flux cases closer to experimental parameters. This is encouraging for the future experimental validation of the QuaLiKiz model and for extrapolation to ITER. Transport in ITER at low magnetic shear will be important for all scenarios, due to the predicted ITER sawtooth period being significantly higher than the energy confinement time.

ACKNOWLEDGMENTS

This work, supported by the European Communities under the contract of Association between EURATOM/FOM and EURATOM/CEA, was carried out within the framework of the European Fusion Programme with financial support from NWO. The views and opinions expressed herein do not necessarily reflect those of the European Commission. This work is supported by NWO-RFBR Centre-of-Excellence on Fusion Physics and Technology (Grant No. 047.018.002). The authors would like to thank T. Görler, F. Merz, D. Told, and H. Doerk for their support in using GENE; R. Waltz, J. Candy, P. Mantica, G. Staebler, and C. McDevitt for fruitful discussions; J. Kinsey for having providing access to GYRO simulation results. This research used resources of the National Research Scientific Computing Center, which is supported by the Office of Science of the U.S. Department of Energy under Contract No. DE-AC02-05CH11231. The authors are extremely grateful to D. Mikkelsen for having provided computational resources.

APPENDIX A: ANALYTIC FLUID LIMIT

The analytic fluid limit is obtained by considering mode frequencies far above the resonance, i.e., $\omega \gg \omega_d, k_{\parallel} V_{\parallel i}$. This corresponds to driving gradients far above the linear thresholds. We assume an ordering $k_{\perp} \rho_e \ll k_{\perp} \rho_i \ll 1$ and $k_{\perp} \delta_e \ll k_{\perp} \delta_i \ll 1$, as well as adiabatic passing electrons, large-aspect-ratio, $\alpha = 0$, and strongly ballooned eigenfunctions centered around the equatorial midplane. The fundamental linear gyrokinetic dispersion equation can then be simplified to the following:¹⁴

$$\left[1 + \frac{n^2 \omega_{pe}^* \omega_d (f_i + \frac{\pi}{Z})}{f_p \omega^2} - \frac{n \omega_{ne}^*}{\omega} + \frac{n \omega_d}{\omega} \right. \\ \left. + \left(-\frac{k_{\parallel}^2 c_{eff}^2}{2 \omega^2} + \frac{k_{\perp}^2 d_{eff}^2}{2} \right) \left(1 + \frac{\tau n \omega_{pe}^*}{Z \omega} \right) \right] \tilde{\phi} = 0, \quad (\text{A1})$$

where $\rho_{i,e}$ and $\delta_{i,e}$ are the particle Larmor radii and banana widths, n is the toroidal wave number, $\omega_d = -\frac{k_\theta T_s}{e_s B} (\cos \theta + s\theta \sin \theta)$ is the vertical drift frequency, $\omega_{ne}^* = -\frac{k_\theta T_s}{e_s B} \frac{1}{L_n}$ and $\omega_{pe}^* = -\frac{k_\theta T_s}{e_s B} \frac{1}{L_p}$ are the diamagnetic frequencies associated with the density and pressure gradient lengths, respectively, $V_{\parallel i}$ is the ion parallel velocity, $\tau = \frac{T_i}{T_e}$, Z is the effective ion charge, $f_{t,p}$ are the trapped and passing particle fractions, respectively, $c_{eff}^2 \equiv \frac{T_e}{m_p}$, and $d_{eff}^2 \equiv \frac{f_p T_e}{f_c n_e} \sum_i \frac{n_i Z_i^2}{T_i} \delta_i + \frac{4T_e m_p}{e^2 B^2}$. In the limit where $q(r) \approx q(r_0) + q'(r_0)x$, we can write $k_{\parallel} = k'_{\parallel} x = k_\theta x / L_s$, where $x \equiv (r - r_0)$ (the distance from the rational surface) and $L_s \equiv Rq/s$. Transforming the radial coordinate from Fourier space to real space, we can also write $k_{\perp}^2 = k_\theta^2 - d^2/dx^2$. Equation (A1) is then a second order differential equation for $\tilde{\phi}(x)$. A Gaussian solution, $\tilde{\phi} = \phi_0 e^{-\frac{x^2}{2w^2}}$, with $w^2 = -\frac{i\omega_d d_{eff} L_s}{k_\theta c_{eff}}$, implies that $\tilde{\phi}'' = -(\frac{1}{w^2} + \frac{1}{w^4} x^2) \tilde{\phi}$, and thus imposes a quadratic equation for the solution of the growth rate $\gamma = nIm(\Omega)$, with $\Omega = \omega/n$

$$\Omega^2 \left(1 + \frac{k_\theta^2 d_{eff}^2}{2} \right) + \Omega \left(-\omega_{ne}^* + \omega_d + i \frac{k_\theta c_{eff} d_{eff}}{nL_s} \right) + \frac{k_\theta^2 d_{eff}^2 \tau}{2} \omega_{pe}^* + \frac{\omega_{pe}^* \omega_d}{f_p} \left(f_t + \frac{\tau}{Z} \right) + \frac{\tau}{Z} \omega_{pe}^* i \frac{k_\theta c_{eff} d_{eff}}{2nL_s} = 0. \quad (\text{A2})$$

To recover the interchange limit, where curvature dominates, we take the ordering $f_p, f_t, \frac{\tau}{Z}, \sim O(1), k_\theta d_{eff}, L_p/R, \frac{(qR/\epsilon^{0.5})}{L_s} \sim O(\delta), L_p/L_n \sim O(\delta^2)$, where ϵ is the inverse-aspect-ratio. In this limit, we obtain for the growth rate

$$\gamma^2 = \frac{(f_t + \frac{\tau}{Z}) n^2 \omega_{pe}^* \omega_d}{f_p} \quad (\text{A3})$$

while for the slab limit, the relevant ordering is $f_p, f_t, \frac{\tau}{Z}, \sim O(1), k_\theta d_{eff}, L_p/R, \frac{L_s}{(qR/\epsilon^{0.5})} \sim O(\delta)$, and $L_p/L_n \sim O(\delta^2)$, which leads to the following expression for the growth rate:

$$\gamma^2 = \frac{\tau n \omega_{pe}^* k_\theta d_{eff} c_{eff}}{2L_s}. \quad (\text{A4})$$

Let us examine the magnetic shear dependence in each of the above limits. For the interchange limit, the s -dependence can be found in ω_d , where $\omega_d \propto \cos \theta + s\theta \sin \theta \Rightarrow \gamma^2 \propto \cos \theta + s\theta \sin \theta$. In the slab limit, since $L_s \equiv Rq/|s|$, we have $\gamma^2 \propto |s|$. In both cases, the growth rates increase with magnetic shear. The fact that the growth rates increase with s in the limit far above the linear instability threshold, while simultaneously the ITG instability threshold also increases with s , points towards reduced growth rate stiffness at lower magnetic shear.

APPENDIX B: LOCALITY APPROXIMATION AT LOW MAGNETIC SHEAR

The QuaLiKiz model is a local code (as are the versions of non-linear GYRO and GENE used here in this

work) and thus assumes constant profile gradient lengths. This can be formulated as $\max(w, d) < \min(L_{n(e,i)}, L_{T(e,i)})$, where w is the mode width, d the distance between rational surfaces, and L_n, L_T the electron or ion density and temperature gradient lengths, respectively. This assumption must fail at a sufficiently low value of s as the distance between rational surfaces grows further and further apart, since $d = 1/sk_\theta$. At low shear, d and w are comparable in the QuaLiKiz model (see Appendix A in Ref. 9). We can estimate this s value as follows: first since d and w are comparable at low shear, we find the s for which $d = L_T$. $\frac{R}{d} = \frac{R}{L_T} \Rightarrow sk_\theta R = \frac{R}{L_T} \Rightarrow s(k_\theta \rho_s) \frac{R}{\rho_s} = \frac{R}{L_T}$. Taking $k_\theta \rho_s = 0.1$, which is approximately the value above which unstable modes are predicted to contribute significantly to the fluxes, and taking a typical R/L_T value of 9, we obtain: $s = 90 \frac{\rho_s}{R}$. For mid-sized tokamaks, a typical value of $\frac{\rho_s}{R}$ is 0.001, thus a typical s for which the locality assumption fails is 0.1, higher for smaller tokamaks and lower for larger tokamaks.

APPENDIX C: ANALYTICAL FLUID EIGENMODE ASSUMPTION

In this appendix, we show, in comparisons with linear-GENE, that the analytical fluid Gaussian eigenmode approximation made in QuaLiKiz and the strong ballooning representation inherent therein are valid for $|s| > 0.1$.

The scale separation of the microinstabilities, where $k_{\parallel} \ll k_{\perp}$, is captured in the eikonal representation for the electrostatic potential perturbation: $\Phi_n(r, \theta, \varphi) = e^{-in(\varphi - q(r)\theta)} \phi_n(r, \theta)$, where ϕ_n has slow varying θ dependence along the field line. To first order $q(r) \approx q(r_0) + xq'|_{r_0}$, with r_0 corresponding to the resonating surface where $q(r_0) = m_0/n$, and $x \equiv r - r_0$, the radial distance from the resonating surface. The poloidal harmonic of Φ_n is thus

$$\tilde{\phi}_{mn}(r) = \frac{1}{2\pi} \int_{-\pi}^{\pi} \phi_n(\theta) e^{i\theta(\frac{\nu}{d} - \nu)} d\theta \quad (\text{C1})$$

with $\nu = m - m_0$, $d = 1/nq'$, and where we have assumed radial dependence only through $q(r)$. In the QuaLiKiz model, $\tilde{\phi}(r)$ is not solved, but prescribed from the fluid limit solution, which is a Gaussian: $\tilde{\phi}(r) = \phi_0 e^{-r^2/2w^2}$, with w the Gaussian width.⁸ The fluid limit solution is outlined in Appendix A. If $\phi_n(\theta)$ vanishes sufficiently quickly at $\pm\pi$, then Eq. (1) describes a Fourier transform. $\phi_n(\theta)$ is then the conjugate of $\phi_n(r)$, with $\theta = k_r d$. However, for low shear and long wavelengths, this assumption may fail since the prescribed $\phi(k_r)$ solution may not be compatible with $\phi(\theta)$ periodicity since then $\phi(\theta)$ may not necessarily vanish at $\pm\pi$. Indeed, it is known that as $s \rightarrow 0$ the full ballooning representation solution of $\phi(\theta)$ tends to a Mathieu function,³⁶ which is not localized in the vicinity $\theta = 0$. Therefore, we expect that below a particular value of s , the QuaLiKiz Gaussian eigenmode assumption must break down.

The validity of the QuaLiKiz assumption that the eigenmode is a Gaussian and vanishing at $\pm\pi$, i.e., $\phi_n(\theta = \pm\pi) \rightarrow 0$, is examined versus the solution of $\phi_n(\theta)$

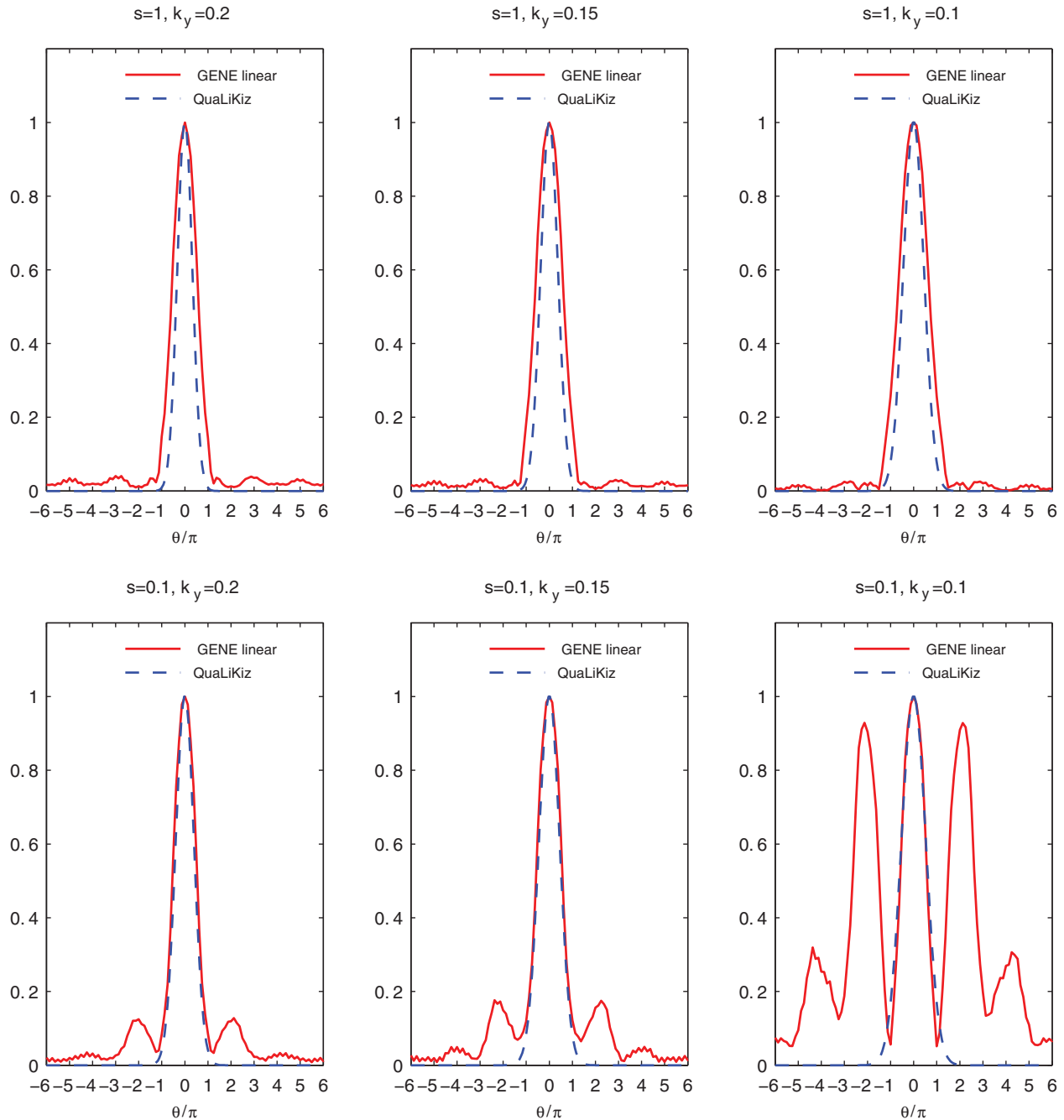


FIG. 16. Calculated GENE linear eigenfunctions compared with the QuaLiKiz strong ballooning assumption for the mode envelope, for $s = 1$ (upper panels) and $s = 0.1$ (lower panels) GASTD case parameters.

from linear GENE, displayed in the ballooning representation.³⁷ The QuaLiKiz/GENE comparison is seen in Figure 16 for the GA standard case at both $s = 0.1$ and $s = 1$. We examine the cases with the transport relevant $k_y = 0.1, 0.15$, and 0.2 . The GENE calculated modes tend to be more extended in the ballooning angle for the combination of low s and low k_y . The QuaLiKiz assumption holds for all cases apart from $s = 0.1$ and $k_y = 0.1$. However, since the peak of the non-linear flux spectrum for the GA-standard $s = 0.1$ case falls between $k_y = 0.15 - 0.2$, the linear calculations for $k_y = 0.1$ are less critical in the low shear case (see Sec. IV C). We can conclude that the lowest order ballooning representation assumption made in QuaLiKiz holds down to $s = 0.1$.

APPENDIX D: IMPROVEMENT IN TRAPPED PARTICLE FUNCTIONAL

QuaLiKiz has been modified to improve the linear growth rate predictions for TEM dominated regimes by including additional terms for the bounce frequency and bounce average treatment in the trapped particle functional. The dispersion relation arising from the linearized Vlasov equation combined with the electroneutrality constraint condition can formally be written as³⁸

$$\sum_s \mathcal{L}_{s,t} + \mathcal{L}_{s,p} = 0, \quad (\text{D1})$$

$\mathcal{L}_{s,t}$ and $\mathcal{L}_{s,p}$ are trapped and passing particle functionals for each species, given as

$$\mathcal{L}_{s,p} = \left\langle \int_{-\infty}^{+\infty} \frac{dk dx}{\pi} J_0^2(k_{\perp} \rho_s) |\tilde{\phi}(x, k)|^2 \frac{\omega - n\omega_s^*}{\omega - n\omega_d^p - k_{\parallel} v_{\parallel} + i0^+} \right\rangle_p, \quad (\text{D2})$$

$$\mathcal{L}_{s,t} = \left\langle \sum_m \int_{-\infty}^{+\infty} \frac{dk_r}{2\pi} J_0^2(k_{\perp} \rho_s) J_m^2(k_r \delta_s) |\tilde{\phi}(k_r)|^2 \times \frac{\omega - n\omega_s^*}{\omega - n\omega_d^t - m\omega_b + i0^+} \right\rangle_t. \quad (\text{D3})$$

The integrations $\langle \dots \rangle_{t,p}$ are defined as

$$\begin{aligned} \langle \dots \rangle_t &= \int_0^{+\infty} \frac{2}{\sqrt{\pi}} \sqrt{\mathcal{E} d\mathcal{E}} \int_{\lambda_c}^1 \frac{d\lambda}{4\bar{\omega}_b} \\ &= f_t \int_0^{+\infty} \frac{2}{\sqrt{\pi}} \sqrt{\mathcal{E} d\mathcal{E}} \int_0^1 K(\kappa) \kappa d\kappa, \\ \langle \dots \rangle_p &= \int_0^{+\infty} \frac{2}{\sqrt{\pi}} \sqrt{\mathcal{E} d\mathcal{E}} \int_0^{\lambda_c} \frac{d\lambda}{4\bar{\omega}_b}, \end{aligned} \quad (\text{D4})$$

ω_d^t is the trapped particle vertical drift frequency, taken as $n\omega_d^t = -\frac{k_{\parallel} T_e}{e_s B} f(\kappa)$ where $f(\kappa) = 2\frac{E(\kappa)}{K(\kappa)} - 1 + 4s(\kappa^2 - 1 + \frac{E(\kappa)}{K(\kappa)})$, and $K(\kappa)$ and $E(\kappa)$ are first and second order complete elliptic integrals. $n\omega_d^p$ is the passing particle vertical drift frequency: $n\omega_d^p = -\frac{k_{\parallel} T_e}{e_s B} (\cos \theta + (s\theta - \alpha \sin \theta) \sin \theta)$. ω_s^* is the diamagnetic frequency for the s species, $\omega_b = \pm \frac{V_{Te}}{qR} \sqrt{\mathcal{E} \bar{\omega}_b}$ is the bounce frequency, m is the poloidal wave number, J_m is the m -order Bessel function, and the poloidal harmonic $\tilde{\phi}$ is the eigenfunction (taken from the analytical fluid limit). Finally, $\bar{\omega}_b$ measures the effects of the variation of the pitch angle λ around a poloidal revolution.

In the previous version of QuaLiKiz, only the $m = 0$ term in Eq. (D3) was implemented. In most cases, the $m \neq 0$ terms are negligible contributors to the resonance. However, in some cases—such as at high $|s|$ or for low T_i gradients—the influence of the bounce frequency ω_b on the resonance can be significant. Therefore, the $m = 1$ term has been incorporated in QuaLiKiz.

APPENDIX E: IMPROVEMENT OF THE MODE WIDTH CALCULATION AT HIGH k_y

In this appendix, the modification of the QuaLiKiz mode width calculation for high k_y ETG modes is reviewed. The electrostatic potential eigenmode is not self-consistently calculated in QuaLiKiz, but rather prescribed from a fluid limit analytical calculation as seen in Eq. (1). In this limit, the eigenfrequencies of the unstable modes are considered much greater than the drift and diamagnetic frequencies. Furthermore, $k_y < 1$ when assessing the ordering of the various terms. The dispersion relation is linearized under these assumptions, where Bessel functions containing ion scales are expanded to second order, and

Bessel functions containing electron scales expanded to zeroth order. ϕ is then the Gaussian solution of the resulting second order differential equation. However, for high wave numbers corresponding to ETG modes—typically $k_y > 2$ —the assumptions regarding the linearization of the Bessel functions in the dispersion relation are not satisfied. In this case, we can assume adiabatic ions (equate Bessel functions containing ion scales to zero), and assuming $k_{\theta} \rho_e \ll 1$ expand the Bessel functions containing electron scales to second order. In these conditions, the linearized gyrokinetic dispersion relation reads

$$\begin{aligned} &\left[\frac{Z_{\text{eff}}}{\tau} + \frac{n\omega_{ne}^*}{\omega} - \left(1 - \frac{n\omega_{pe}^*}{\omega} \right) - \frac{n\omega_d}{\omega} + f_p \left(1 - \frac{n\omega_{pe}^*}{\omega} \right) \right. \\ &\quad \left. \times \left(\frac{k_{\perp}^2 d_{\text{eff}}^2}{2} - \frac{n\omega_d}{\omega} (s - \alpha - 0.5) - \frac{k_{\parallel}^2 v_{Te}^2}{2\omega^2} \right) \right] \tilde{\phi} = 0, \end{aligned} \quad (\text{E1})$$

where $d_{\text{eff}} = \frac{f_p}{f_p} \delta_e + \rho_e$ in this case. This equation is similar to Eq. (1), and as in the previous case, the solution for ϕ is a Gaussian whose width w is given by

$$w^4 = -\frac{\omega^2 (d_{\text{eff}}^2 - 2d^2 (s - \alpha - 0.5))}{\left(\frac{k_{\theta} s}{qR} v_{Te} \right)^2}, \quad (\text{E2})$$

where the ratio $\frac{n\omega_d}{\omega}$ is considered equal to 1. We obtain a quadratic equation for ω

$$\begin{aligned} &\Omega^2 \left(\frac{Z_{\text{eff}}}{\tau} + f_p \frac{k_{\theta}^2 d_{\text{eff}}^2}{2} \right) + \Omega \left(\omega_{ne}^* - \omega_d - f_p \frac{k_{\theta}^2 d_{\text{eff}}^2}{2} \omega_{pe}^* \right. \\ &\quad \left. + i f_p \frac{k_{\theta} s v_{Te} d_{\text{eff}}}{2nqR} \right) + \omega_{pe}^* \omega_d - i f_p \frac{k_{\theta} s v_{Te} d_{\text{eff}}}{2nqR} \omega_{pe}^* = 0. \end{aligned} \quad (\text{E3})$$

In the interchange limit, the solution is $\gamma^2 = \frac{n\omega_{pe}^* n\omega_d}{Z_{\text{eff}} \tau}$. In the

slab limit, the solution is $\gamma^2 = \frac{k_{\theta} s v_{Te} d_{\text{eff}} n\omega_{pe}^*}{2qR Z_{\text{eff}} \tau}$.

The new eigenfunction at high k_y has been validated by linear GENE, as seen in Figure 17. The new mode width is much closer to the GENE calculated eigenmode at high k_y . A flag has been implemented in QuaLiKiz to switch between the low k_y and high k_y versions of the linearized dispersion relation for the mode width calculation, based on an assessment of the degree of adiabicity of the passing electrons. This switch is typically triggered within the range $k_y \sim 1 - 2$. The normalized linear growth rates from both GENE and QuaLiKiz, as a function of k_y , can be seen in Figure 18. The scan was carried out for $R/L_{Ti} = 0$ with the remaining parameters corresponding to the GA-standard case. At high k_y , the agreement between linear growth rates of QuaLiKiz and GENE is clearly improved.

This could be of importance for the accurate modelling of ETG modes, which may, for example, be responsible for residual electron transport in transport barriers.

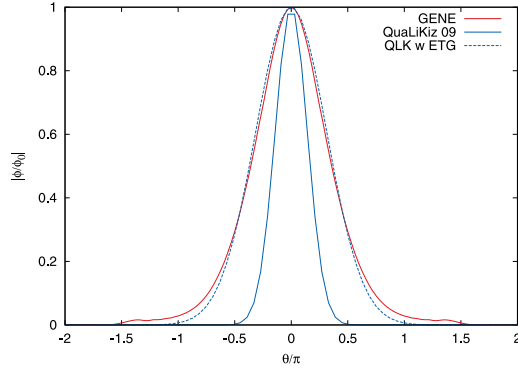


FIG. 17. Electrostatic potentials calculated by GENE and QuaLiKiz for $k_y = 30$.

APPENDIX F: IMPROVEMENT OF THE MODE WIDTH CALCULATION AROUND $s = 0.5$

QuaLiKiz was also modified to correct an inaccuracy of the model in the region $s \sim 0.5$, linked to the mode width calculation. The expression for the linearized gyrokinetic dispersion relation is repeated here

$$\left[1 + \frac{f_t}{f_p} \left(1 + \frac{\tau}{Z} \right) \frac{n\omega_{pe}^* n\omega_d^f}{\omega^2} - \frac{n\omega_{ne}^*}{\omega} + \left(1 + \frac{\tau}{Z} \frac{n\omega_{pe}^*}{\omega} \right) \left(\frac{n\omega_d^p}{\omega} - \frac{k_{\parallel}^2 c_{eff}^2}{2\omega^2} + \frac{k_{\perp}^2 d_{eff}^2}{2} \right) \right] \tilde{\phi} = 0, \quad (\text{F1})$$

where f_t and f_p are the fraction of trapped and passing particles, respectively, d_{eff} is an effective banana width, which takes into account finite Larmor radius (FLR) and finite banana width (FBW) effects: $d_{eff}^2 = \rho_{eff}^2 + f_t/f_p \delta_{eff}^2$, where $\rho_{eff}^2 = \frac{4T_e m_p}{e^2 B^2}$ is the effective Larmor radius and $\delta_{eff}^2 = \frac{q^2}{2e} \rho_{eff}^2$ is the effective banana width. $c_{eff} = \sqrt{\frac{T_e}{m_p}}$ is the effective thermal velocity and $\frac{\tau}{Z} = \sum_i \frac{\nabla_r P_i}{\nabla_r P_e}$ is the ratio of the pressure gradients between electrons and ions. The diamagnetic frequency has been split into two terms: one due to the density gradients— $n\omega_{ns}^* = -\frac{k_{\theta} T_s}{e_s B} \frac{d}{dr} \log n_s$ —and one due to the pressure gradients— $n\omega_{ps}^* = -\frac{k_{\theta} T_s}{e_s B} \left(\frac{d}{dr} \log n_s + \frac{d}{dr} \log T_s \right)$.

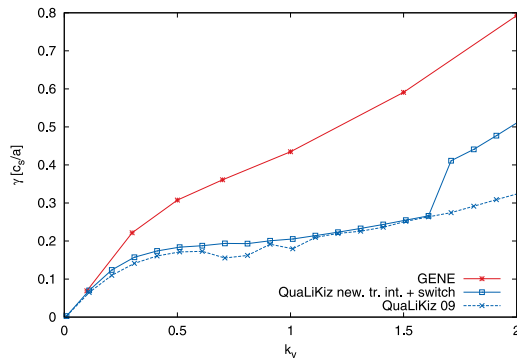


FIG. 18. Linear growth rates calculated by GENE and QuaLiKiz for the $R/L_{T_i} = 0$ scenario.

Note that Eq. (F1) is identical to Eq. (A1) apart from the separation of $n\omega_d$ into distinct trapped and passing particle expressions. This is due to the fact that $n\omega_d^p$ and $n\omega_d^f$ are identical only to 0th order in θ . The passing particle expression is

$$n\omega_d^p = -\frac{k_{\theta} T_s}{e_s B R} (\cos \theta + (s\theta - \alpha \sin \theta) \sin \theta), \quad (\text{F2})$$

whereas the expression of $n\omega_d^f$ in the deeply trapped limit is $n\omega_d^f = -\frac{k_{\theta} T_s}{e_s B R} = n\omega_d$. When expanding ω_d^p to second order in θ , we obtain

$$n\omega_d^p = -\frac{k_{\theta} T_s}{e_s B R} (1 + \theta^2 (s - \alpha - 0.5)). \quad (\text{F3})$$

Equation (1) is the same as Eq. (1) apart from the following term, proportional to s : $\left(1 + \frac{\tau}{Z} \frac{n\omega_{pe}^*}{\omega} \right) \frac{n\omega_d}{\omega} (k_r d)^2 (s - \alpha - 0.5)$. This leads to a modified expression for w compared to the expression presented in Appendix A⁹

$$w^4 = -\frac{\left(d_{eff}^2 + 2 \frac{f_t}{f_p} d^2 (s - \alpha - 0.5) \right) \omega^2}{\left(\frac{k_{\theta} s}{qR} c_{eff} \right)^2}, \quad (\text{F4})$$

where the ratio $\frac{n\omega_d}{\omega}$ has been taken equal to 0.5.

With this definition for w , the divergence issue mentioned in Ref. 8 around $s = 0$ is resolved. However, there is still an irregularity around $s = 0.5$ as can be seen in the dashed curve in Figure 19. This effect is shown for $k_y = 0.3$ as an example, but this irregularity is present for all wave numbers, although somewhat smoother at greater k_y . This irregularity stems from the second order expansion the vertical drift frequency $n\omega_d^p$.

In the current version of QuaLiKiz, $n\omega_d^p$ was expanded to sixth order in θ . The higher order expansion removes the irregularity at $s = 0.5$ as seen in the solid curve in Figure 19. The new expression for $n\omega_d^p$ is now:

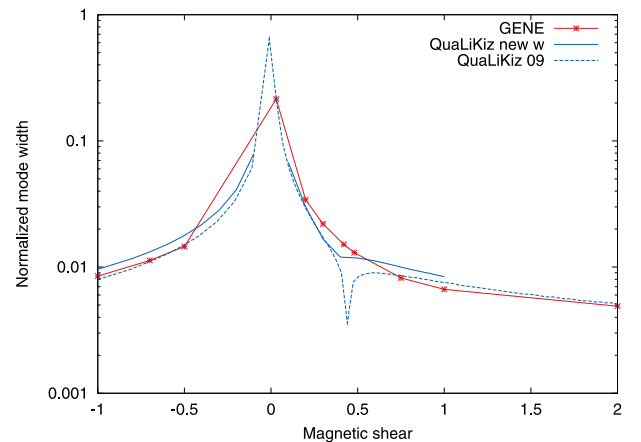


FIG. 19. Mode width (normalized to the minor radius) calculated by GENE and QuaLiKiz for $k_y = 0.3$.

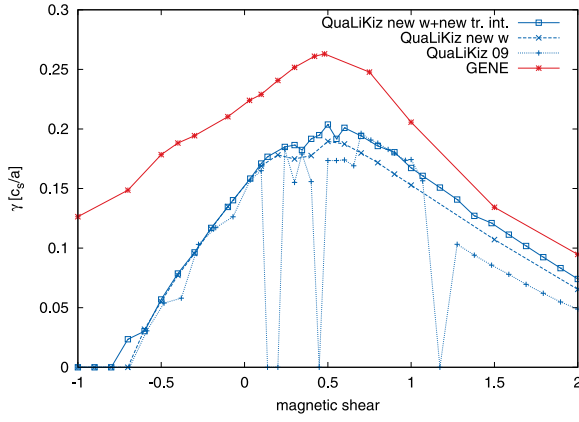


FIG. 20. Linear growth rates of GENE and QuaLiKiz for the GA-standard case (apart from $r/a = 0.25$) at $k_y = 0.3$.

$$n\omega_d^p = n\omega_d \left[1 + \theta^2(s - \alpha - 0.5) - \frac{\theta^4}{6}(s - 2\alpha - 0.25) + \frac{\theta^6}{120} \left(s - \frac{16}{3}\alpha - \frac{1}{6} \right) \right]. \quad (\text{F5})$$

This leads to a new recursive expression for w

$$w^4 = - \left(\frac{\omega d_{eff}}{k_{\theta} s} \right)^2 \left[1 + 2 \frac{f_i d^2}{f_p d_{eff}^2} (s - \alpha - 0.5) + \frac{d^2}{w^2} (s - 2\alpha - 0.25) + \frac{5}{80} \frac{d^4}{w^4} (6s - 32\alpha - 1) \right]. \quad (\text{F6})$$

All improvements implemented in QuaLiKiz are summarized in Figure 20. A scan in magnetic shear is presented with the different versions of QuaLiKiz for GA-standard case parameters, but at reduced radius: $r/a = 0.25$. The dotted curve represents the version of QuaLiKiz used in Ref. 4, the dashed curve illustrates the improvements brought by the new developments of the mode width. The solid curve is the result when the new term for trapped particles is added. Figure 20 was chosen to be plotted for $k_y = 0.3$, a typical wavenumber contributing significantly to the transport flux. However, the improvements due to the new high- k_y calculation are thus not evident from this graph, but those improvements are evident in Figure 18.

¹C. Bourdelle, X. Garbet, F. Imbeaux, A. Casati, N. Dubuit, R. Guirlet, and T. Parisot, *Phys. Plasmas* **14**, 112501 (2007).

²J. Candy and R. Waltz, *J. Comput. Phys.* **186**, 545 (2003).

³J. Candy and R. Waltz, *Phys. Rev. Lett.* **91**, 045001 (2003).

⁴A. Casati, C. Bourdelle, X. Garbet, F. Imbeaux, J. Candy, F. Clairet, G. Dif-Pradalier, G. Falchetto, T. Gerbaud, V. Grandgirard, Ö. Gürçan, P. Hennequin, J. Kinsey, M. Ottaviani, R. Sabot, Y. Sarazin, L. Vermare, and R. Waltz, *Nucl. Fusion* **49**, 085012 (2009).

⁵P. Mantica, C. Angioni, C. Challis, G. Colyer, L. Frassinetti, N. Hawkes, T. Johnson, M. Tsalas, P. C. deVries, J. Weiland, B. Baiocchi, M. Beurskens, A. Figueiredo, C. Giroud, J. Hobirk, E. Joffrin, E. Lerche, V. Naulin, A. Peeters, A. Salmi, C. Sozzi, D. Stryntzi, G. Staebler, T. Tala, D. V. Eester, and T. Versloot, *Phys. Rev. Lett.* **104**, 135004 (2011).

⁶F. Porcelli, D. Boucher, and M. Rosenbluth, *Plasma Phys. Controlled Fusion* **38**, 2163 (1996).

⁷F. Jenko, W. Dorland, M. Kotschenreuther, and B. Rogers, *Phys. Plasmas* **7**, 1904 (2000).

⁸C. Bourdelle, X. Garbet, G. Hoang, J. Ongena, and R. Budny, *Nucl. Fusion* **42**, 892 (2002).

⁹M. Romanelli, G. Regnoli, and C. Bourdelle, *Phys. Plasmas* **14**, 082305 (2007).

¹⁰A. Casati, Ph.D. dissertation, Universite de Provence (Aix-Marseille I), 2009.

¹¹A. Casati, T. Gerbaud, P. Hennequin, C. Bourdelle, J. Candy, F. Clairet, X. Garbet, V. Grandgirard, Ö. Gürçan, S. Heuraux, G. Hoang, C. Honoré, F. Imbeaux, R. Sabot, Y. Sarazin, L. Vermare, and R. E. Waltz, *Phys. Rev. Lett.* **102**, 165005 (2009).

¹²F. Jenko, T. Dannert, and C. Angioni, *Plasma Phys. Controlled Fusion* **47**, B195 (2005).

¹³J. Kinsey, R. Waltz, and J. Candy, *Phys. Plasmas* **13**, 022305 (2006).

¹⁴C. Bourdelle, Ph.D. dissertation, Universite Joseph Fourier-Grenoble 1, 2000.

¹⁵S. Guo and F. Romanelli, *Phys. Fluids B* **5**, 520 (1993).

¹⁶M. Romanelli, C. Bourdelle, and W. Dorland, *Phys. Plasmas* **11**, 3845 (2004).

¹⁷C. Fourment, G. Hoang, L.-G. Eriksson, X. Garbet, X. Litaudon, and G. Tresset, *Plasma Phys. Controlled Fusion* **45**, 233 (2003).

¹⁸A. Casati, C. Bourdelle, X. Garbet, and F. Imbeaux, *Phys. Plasmas* **15**, 042310 (2008).

¹⁹F. Jenko, W. Dorland, and G. Hammett, *Phys. Plasmas* **8**, 4096 (2001).

²⁰F. Romanelli, L. Chen, and S. Briguglio, *Phys. Fluids B* **3**, 2496 (1991).

²¹R. Kubo, *J. Math. Phys.* **4**, 174 (1963).

²²J. Krommes, *Phys. Rep.* **360**, 1 (2002).

²³D. Escande and F. Sattin, *Phys. Rev. Lett.* **99**, 185005 (2007).

²⁴Z. Lin, I. Holod, L. Chen, P. Diamond, T. Hahm, and S. Ethier, *Phys. Rev. Lett.* **99**, 265003 (2008).

²⁵T. Dannert and F. Jenko, *Phys. Plasmas* **12**, 072309 (2005).

²⁶P. Diamond, S.-I. Ito, K. Itoh, and T. Hahm, *Plasma Phys. Controlled Fusion* **47**, R31 (2005).

²⁷R. Waltz, G. Staebler, W. Dorland, G. Hammett, M. Kotschenreuther, and J. Konings, *Phys. Plasmas* **4**, 2482 (1997).

²⁸J. Kinsey, G. Staebler, and R. Waltz, *Phys. Plasmas* **12**, 052503 (2005).

²⁹J. Kinsey, G. Staebler, and R. Waltz, *Phys. Plasmas* **15**, 055908 (2008).

³⁰T. Hahm, M. Beer, Z. Lin, G. Hammett, W. Lee, and W. Tang, *Phys. Plasmas* **6**, 922 (1999).

³¹L. Jiquan and Y. Kishimoto, *Phys. Plasmas* **12**, 054505 (2005).

³²F. Hinton and G. Staebler, *Phys. Fluids B* **5**, 1281 (1993).

³³R. Waltz, A. Casati, and G. Staebler, *Phys. Plasmas* **16**, 072303 (2009).

³⁴D. Hatch, P. Terry, W. Nevins, and W. Dorland, *Phys. Plasmas* **16**, 022311 (2009).

³⁵D. Hatch, P. Terry, F. Jenko, F. Merz, and W. Nevins, *Phys. Rev. Lett.* **106**, 115003 (2011).

³⁶J. Candy, R. Waltz, and M. Rosenbluth, *Phys. Plasmas* **11**, 1879 (2004).

³⁷J. Connor, R. Hastie, and J. Taylor, *Phys. Rev. Lett.* **40**, 396 (1978).

³⁸X. Garbet, L. Laurent, F. Mourgues, and J. P. Samain, *J. Comput. Phys.* **87**, 249 (1990).